

FINAL REPORT

**STATISTICS AND VARIABILITY OF TURBULENCE DYNAMICS IN THE
MIDDLE ATMOSPHERE**

AFOSR GRANT F49620-02-1-0026

Alex Mahalov and Basil Nicolaenko
Principal Investigators
Department of Mathematics
Department of Mechanical and Aerospace Engineering
Program in Environmental Fluid Dynamics
Arizona State University
Tempe, AZ 85287-1804
e-mail: byn@stokes.la.asu.edu, mahalov@asu.edu

20050728 098

Project objectives related to ABL-ADA (Atmospheric Decision Aid):

- modeling and parametrization of coupled mechanical and optical turbulence in the middle atmosphere, for the Air Force Airborne Laser (ABL) Program and; compact laser systems;
- multiparameter non-equilibrium anisotropic turbulence models incorporating both vertical and horizontal structures: improved modeling of anisotropic C_n^2 for the Air Force ABL Program and other directed energy platforms; parametrization of vertical C_n^2 profiles;
- multiple scaling branches for the parametrization of turbulence outer length scales in stratospheric shear-stratified turbulence;
- parametrization and vertical variability of turbulence outer length scales, temperature fluctuations and related physical quantities required for propagation codes; “catalogue” for a representative set of atmospheric events around the tropopause, of relevance to ABL/ADA;
- benchmarking of such models for strong anisotropic intermittencies against experimental field data for the Air Force ABL Program;
- microscale stratospheric turbulence codes coupled with mesoscale dynamics;
- correlation with mesoscale atmospheric dynamics (WRF, MM5 codes), data from the latter to be inputted on a coarse grid;
- system performance modeling and determination of performance bounds via simulation of both average atmospheric events and more extreme atmospheric events of relevance to ABL-ADA.

Project objectives for Stratospheric Clear Air Turbulence (CAT)

- Resolve physics of higher altitude stratospheric CAT which occurs under conditions of strong stable background stratification and is very different from the CAT at lower altitudes, dominated by convective instabilities;
- characterization of stratospheric CAT at elevations of 55,000–70,000 ft.; wave induced wind shear in synergy with saturated inertio-gravity wave field;
- microscale physics of thin layers of stratospheric CAT induced by lateral shear generated by gravity waves in the stratosphere;
- production runs on massively parallel architectures with high resolution 3D DNS simulations resolving thin CAT layers (anelastic and incompressible microscale codes with adaptive nonuniform vertical gridding);
- resolution of strong energetic eddies with typical vertical scales of a few hundred meters;
- propagation of gravity waves of long period and short vertical wavelength generating mechanical lateral shear;
- construction of tables of multi-valued scaling relations and multiple branches parameterizations for length and rms velocity scales for a catalogue of representative stratospheric field conditions;
- parameterization of eddy mixing coefficients of momentum and heat in the lower stratosphere;
- incorporation of the above into real-time AFWA operational models for stratospheric CAT forecasting as well as to the next generation mesoscale WRF code.

1 Summary of Accomplishments

- Implementation on massively parallel architectures of an adaptive grid microscale code for turbulence around the atmospheric tropopause and the lower stratosphere (full 3D Navier-Stokes Boussinesq equations).
- Implementation of a microscale code for the full 3D Navier-Stokes Anelastic equations for turbulence in the lower stratosphere.
- Simulation of the Vandenberg field campaign (strong jet in California): calibration and comparison with field measurements.
- Characterization of quasi-equilibrium dynamics of stratified turbulence around tropospheric jets.
- Statistics and variability of turbulence outer length scales in the above cases.
- Evidency of layers (above and below edges of jet stream) of strong variability of the refractive index C_n^2 in agreement with observations.
- Regime transitions from shear-dominated (inner core) → buoyancy affected (jet flanks) → buoyancy dominated turbulence along a jet stream.
- Multi-valued scaling branches, with respect to local gradient Richardson number (Ri_g) are demonstrated for shear stratified turbulence outer scales and other turbulence statistics quantities.
- Two distinct scaling curves for the upper and lower flanks of jet, with branch switching at critical heights.
- Critical heights correspond to vertical levels of maximal shearing in the turbulent *mean* velocity profile of the jet (inflection points criteria).
- Shear, Tatarskii and buoyancy scales should be used in combination for the parameterization of enhanced layers of C_n^2 , not just the buoyancy (Deardorff) outer scale.
- Simulation of strong CAT events induced by gravity waves in the stratosphere at 60,000–70,000 ft.
- Two sets of simple power scaling laws for Tatarski outer length scale vs. (Ri_g): payoff in simple parametrization of outer scale for C_n^2 -formula in ABL-propagation codes.
- Stratospheric CAT is related to shear instability associated with gravity waves (lateral directional shear is the key instability mechanism);
- Stratospheric CAT layers around 20,000m altitude are dominated by strong energetic eddies with typical horizontal scale $\sim 500m$ (these eddies are not resolved in simulations with MM5 and WRF mesoscale codes);

- rms fluctuating vertical velocity in CAT layers is of the same order as the mean horizontal wind speed; strikingly, we find the same 4.5m/s range measured by Vernin et al, and our fine vertical gridding yields higher local peaks of 7 m/s for the vertical velocity fluctuations;
- Such stratospheric CAT layers cannot be resolved in mesoscale meteorological codes such as MM5 and WRF.

2 Technical Report: ABL issues

This project falls within the realm of the USAF mission of developing air defense systems, a component of which is the ongoing Airborne Laser (ABL) Program. The recent congressional mandate to develop an airborne missile defense system for the US will bolster the ABL program, since laser technology is a viable tool for such an effort. One of the major challenges of the ABL program is the development of laser-beam propagation codes. Such codes must account for the beam propagation through an extended turbulent medium, consisting of the bulk of the troposphere and stratosphere. From the operational perspective (Atmospheric Decision Aid, ADA), rigorous modeling of the refractive index structure function for long horizontal or nearly horizontal paths under high scintillation conditions characteristic of the atmosphere is imperative. In spite of demonstrated importance of stratification on atmospheric optical turbulence, currently available ABL phase screen theories hinge upon isotropic Kolmogorov spectrum (Rytov's theory), and hence cannot represent large amplitude fluctuations of atmospheric stratified turbulence. In the context of such turbulence the collusion between the stratification and shear leads to many intriguing phenomena such as the formation of thin, elongated turbulent layers (pancakes) and instabilities (such as Kelvin-Helmholtz (K-H) billowing, Figure 13) that ultimately break down into turbulence. The turbulence so generated is often patchy and temporally intermittent, characterized by strong anisotropy. It produces strong optical scintillation due to refractive index fluctuations, which needs to be quantified accurately in developing advanced beam control concepts for atmospheric laser-beam propagation.

2.1 Overview

Clear air turbulence (CAT) in the free atmosphere is of importance in meteorology, aviation industry, and remote sensing applications. Kelvin-Helmholtz instability (KHI) is known to be responsible for a large fraction of CAT occurring in association with jet streams near the tropopause, when synoptic conditions are favorable (Bedard et al. 1986; Chilson et al. 1997; Pavelin et al. 2001, 2002; Luce et al. 2002; Yamamoto et al. 2003). We also note that other mechanisms of CAT include localized shear instabilities due to gravity waves (generated either by mountains or geostrophic adjustment at upper level frontal zones) or gravity wave breaking (cf. Clark et a. 2000; Pavelin et al. 2001), deep tropospheric convection

(cf. Lane et al. 2003) etc. KHI mechanism, relevant for the atmosphere, is a dynamical instability which occurs in a stably stratified, shear flow when there is an inflection point in the mean velocity profile and the associated wind shear is sufficiently strong. The primary external parameter associated with stably stratified, shear flows is the local gradient Richardson number, $Ri_g = N^2/S^2$, where N is the Brunt-Väisälä (or buoyancy) frequency and S is the mean wind shear. Local normalized N^2 exhibits a fine structure across the tropopause (Figure 1). Linear inviscid stability results give $Ri_g > 1/4$ as a sufficient condition for stability of a stratified shear flow (Drazin and Howard 1966). If $Ri_g < 1/4$ locally, unstable modes (or billows), oriented perpendicular to the shear vector (with the vorticity dominated by its spanwise component), may grow extracting energy from the mean flow, and eventually cascade this energy nonlinearly on to a range of smaller scale eddies (Figure 2). KHI billowing usually takes the form of a series of roll vortices separated by thin braids. The billows in the atmosphere typically have a horizontal wavelength of $O(1 \text{ km})$, and vertical thickness of $O(10 \text{ m} - 100 \text{ m})$, which are also the scales on which aircraft bumpiness occur (Sekioka 1970). The horizontal extent of these billows are normally $O(1 \text{ km}-10 \text{ km})$ and life-times few tens of minutes or at most few hours (Browning 1971). The above scale considerations show that KHI occurs mostly in the subgrid scales of current operational mesoscale models. Because KHI mechanism is also responsible for a significant amount of vertical exchanges of momentum, heat and constituents, it is important to parameterize these processes in mesoscale or large-scale models of the atmosphere (cf. chapters by Cullen 2002 and Babin, Mahalov, Nicolaenko 2002 in the monograph *Large-Scale Atmosphere-Ocean Dynamics*, 2002, Cambridge University Press),

On the other hand, *optical* (or refractive index) *turbulence* (OT), detected by radars and radiosondes in clear air, is the result of refractive index inhomogeneities. A measure of the intensity of OT is the refractive index structure constant (C_n^2) given by (Tatarski 1961):

$$C_n^2 = a M^2 L_{out}^{4/3}, \quad (1)$$

where a is a constant (generally taken as 2.8), L_{out} is an outer length scale of turbulence (defined as the scale at which Kolmogorov's isotropic, homogeneous, (statistically) stationary inertial range ceases to be valid), M is the gradient of the generalized potential refractive index, which for the upper troposphere and above, is given by (cf. Beland 1993):

$$M^2 = \left(\frac{79 \times 10^{-6} P}{g T} \right)^2 N^4. \quad (2)$$

In Eq. (2), T is the absolute temperature in $^{\circ}\text{K}$, P is the pressure in mb, g is the acceleration due to gravity, and N is the buoyancy frequency given by, $N^2 = (g/\Theta)(d\Theta/dz)$, where the potential temperature Θ is defined as $\Theta = T(1000/P)^{0.286}$ (for air). The following equation relates the structure function for temperature, C_T^2 , to C_n^2

$$C_n^2 = \left(\frac{79 \times 10^{-6} P}{T^2} \right)^2 C_T^2. \quad (3)$$

Turbulence associated with the midlatitude jet stream (cf. Figure 13) is known to support persistent layering of C_n^2 , with vertical scales of $O(1 \text{ m} - 100 \text{ m})$ (cf. Nastrom and Eaton

2001; Luce et al. 2002). It is important to note, from Eq. (1) and Eq. (2), that for an adiabatic (or neutral) layer formed through mechanical turbulent mixing, there will be moderate refractivity fluctuations. Hence, the turbulent layer will be *invisible* to the radar, and it is the edges of these turbulent layers (where Θ -gradients concentrate) that are detected by the radar as optical turbulence (OT). It is clear that care is needed to associate the locations of OT with those of mechanical CAT relevant for aircraft operations. A noteworthy finding by Bedard et al. (1986) is that aircraft turbulence reports came from the inner jet-core region (which includes the jet centerline, where a local increase in Ri_g can also be seen) of a strong tropopause jet. Although *in situ* balloon or aircraft or dropsonde measurements can give us direct measurements of meteorological variables at the tropopause, their value is limited by the few number of samples possible. On the other hand, output fields from current mesoscale atmospheric models are of relatively coarse resolution, and also suffer from uncertainties associated with invalidated subgrid parameterization schemes. In the context of OT, very little is known about the variability of L_{out} near the tropopause, and it acutely requires a good parameterization for use in electromagnetic wave propagation studies (Eaton and Nastrom 1998).

Our forced, high resolution, three-dimensional (3D) numerical simulations, conducted at a resolution of $(512 \times 512 \times 1024)$ on massively parallel architectures, may be interpreted either as the direct numerical simulation (DNS) of a scaled-down model tropopause jet or as the large-eddy simulation (LES), with constant eddy viscosity and diffusivity, of a realistic tropopause jet (resolving vertical scales $O(1 \text{ m}-100 \text{ m})$ and horizontal scales $O(0.1 \text{ km}-1 \text{ km})$ which are most pertinent to CAT or OT near the tropopause); this is published in Mahalov, Nicolaenko, Tse and Fernando 2001, Joseph, Mahalov, Nicolaenko and Tse 2003, 2004.

In a thin fully 3-dimensional computational box centered at the tropopause, these equations are the incompressible Navier-Stokes equations for the velocity \mathbf{U} and temperature Θ , which, under the Boussinesq approximation can be written as:

$$\frac{\partial U}{\partial t} + \mathbf{U} \cdot \nabla U = -\frac{\partial P}{\partial x} + fV + \nu \nabla^2 U + \Pi_U, \quad (4)$$

$$\frac{\partial V}{\partial t} + \mathbf{U} \cdot \nabla V = -\frac{\partial P}{\partial y} - fU + \nu \nabla^2 V, \quad (5)$$

$$\frac{\partial W}{\partial t} + \mathbf{U} \cdot \nabla W = -\frac{\partial P}{\partial z} + \nu \nabla^2 W + g\beta(\Theta - \Theta_R), \quad (6)$$

$$\frac{\partial \Theta}{\partial t} + \mathbf{U} \cdot \nabla \Theta = \kappa \nabla^2 \Theta + \Pi_\Theta, \quad (7)$$

$$\nabla \cdot \mathbf{U} = 0, \quad (8)$$

where $\mathbf{U} = (U, V, W)$ are the three components of the velocity in the streamwise, spanwise and vertical directions (denoted as x,y,z) respectively, Θ_R is the reference temperature (vertically dependent profile); P is the pressure; ν , κ , f , β and g are the molecular viscosity, molecular diffusivity, Coriolis parameter, thermal expansion coefficient and gravitational constant, respectively. The horizontally homogeneous terms Π_U and Π_Θ are the vertically

dependent momentum and thermal sources. The two source terms enable a basic (unstable) jet stream profile and the vertically variable Brunt-Väisälä frequency profile. Due to inhomogeneity in the vertical direction, periodic boundary conditions are not used therein. Note that previous studies have assumed periodicity in the vertical direction. Furthermore, in our simulations, non-linear shear and stratification profiles adjust to roughly stationary values, around which the potential and kinetic energies fluctuate.

With the support of the DoD HPC Challenge Program, we have used spectral domain decomposition methods to perform simulations of shear-stratified turbulence on massively parallel architectures with a particular emphasis on modeling atmospheric jets in the tropopause region. The main difference with the previous numerical studies is that we use more realistic boundary conditions in the vertical direction and the shear and stratification profiles can adjust when the flow evolves. In our simulations, microscale Reynolds number and other turbulent quantities fluctuate within 5% of their mean value. Since the system can adjust to the point where production is balanced by dissipation and diffusion, detailed studies of the budget terms become possible. This is in contrast with the previous numerical studies where the microscale Reynolds number is temporally evolving except at a certain 'stationary' Richardson number for which the growth is balanced by dissipation.

We use a spectral domain decomposition method which is particularly suitable for simulations of flows with non-uniform background stratification and shear. The flow is assumed to be homogeneous only in the horizontal directions where periodic boundary conditions are used for turbulent fluctuations. For each horizontal wavenumber, the vertical domain is then broken down into several subdomains. Further details on the numerical method are given in Mahalov, Nicolaenko, Tse & Fernando (2001). Resolution is $512 \times 512 \times 1024$ on the DoD massively parallel SGI's and IBM P-4 (up to 256 processors).

The physics of subgrid-scale processes must be first understood before they can be represented correctly in larger scale atmospheric models (i.e. the problem of parameterization). The resolved scales in the present simulations belong to the subgrid scales of large-scale/mesoscale models of the atmosphere. An important feature of our simulations is that the background stratification and shear profiles are inhomogeneous (in vertical), and they interact nonlinearly with the perturbation field (i.e. mean wind and temperature profiles are allowed to vary in time). Moreover, integrations are carried out until a quasi-equilibrium state (i.e. when profiles of turbulent mean statistics and budgets remain quasi-stationary in time) is reached. Further, robustness of results is demonstrated through another simulation for which the turbulence budgets are nearly balanced on each vertical level.

The results of Joseph, Mahalov, Nicolaenko and Tse (2003, 2004) provide a useful conceptual picture for the transitions between inhomogeneous flow regimes (in vertical), surrounding a turbulent tropopause jet, through various outer length scale cross-overs. The main focus is on turbulence scaling behaviors pertinent to these inhomogeneous flow regimes. It is demonstrated that multi-valued scaling branches are typical of the scalings of most turbulent quantities examined. One important result of the work is the identification of simple criteria, based on the shear of the turbulent mean jet velocity profile, in order to delineate all

of the multi-valued scaling branches (four of them) in an unambiguous manner. The criteria simply depend on levels of inflection points, and shear minima in the quasi-equilibrium mean jet profile. The application to the Tatarski's outer scale formula (1) should pay-off in robust parameterization of vertical variability of C_n^2 profiles for the ABL/ADA effort.

2.2 Statistics, budgets and simulated fields

We describe the essential features of the simulated turbulent fields. In Fig. 3, we show vertical profiles of several turbulent quantities at the quasi-equilibrium stage of the simulation (with $256^2 \times 1024$ resolution; referred to as *control* simulation). Sensitivity of simulated profiles to variations in the forcing profiles, and some complimentary results are found in Joseph et al. (2003). See the Appendix for definitions of parameters. Since the quasi-equilibrium mean velocity profile shows inflection points (IP) on either sides of the jet (Figs. 3a-b), and $Ri_g < 0.25$ in a large region around their neighborhoods (Fig. 3d), one may expect that the primary instability, in the transition to turbulence, might have occurred as two interacting trains of KHI billows on either sides of the jet. The temperature variance, its dissipation ($\epsilon_\theta = D_\theta$, cf. Appendix) and the total temperature gradients attain local peaks at the edges of the mixing layer (Fig. 3c). Hence, radar echo power (of specific interest to optical turbulence) is expected to maximize along the upper edge of the mixing layer where all the above noted peaks are dominant than those on the lower flank of the jet (an effect of asymmetric stratification). In contrast, the peak in $\langle |w'|^2 \rangle$ (a quantity of primary interest to aircraft bumpiness) occurs at the center of the jet, which is neither the level where radars may detect OT nor the level of 'visible' KHI billows. The central peak of $\langle |w'|^2 \rangle$ is consistent with observations of aircraft turbulence within the inner jet-core (cf. Bedard et al. 1986). Further, in agreement with the present Ri_g profile (cf. Fig. 3d), Bedard et al. (1986) also found that the minimum values of Ri_g (which are less than 0.25) occur at the sides of the jet, while a clear increase of Ri_g , to at least O(10), has been noticed at the centerline of the jet (their Fig. 4). Other evidence for collapse of shear at the core of jets may be found in Fig. 8 and Fig. 9 of Nastrom and Eaton (2001). The above comparisons provide a satisfactory benchmarking of our simulation results against real observations, so that one can examine turbulence scalings.

Next, we have demonstrated that results reported in our study are resolution independent. We have compared profiles of variances and some nondimensional numbers with different horizontal and vertical resolutions. With the exception of minor details, all features in the profiles are preserved, quantitatively.

2.3 Multiple scalings

With ABL applications in mind, we focus on turbulence scalings with the gradient Richardson number, Ri_g (which is also an outer scale ratio, cf. the Appendix for definitions). It is recognized that Ri_g is a useful parameter for representing buoyancy and shear effects in

inhomogeneously stably stratified, shear flows. Ri_g depends only on the large-scale flow parameters readily available from mesoscale models or observations. All the scaling results, for the control simulation, are reported with the higher resolution dataset. For scaling purposes, we concentrate only on the best resolved region of our simulation, which is demarcated by $Ri_g < 10$. This corresponds to data points within the range: $-4.4 < Z < 4.1$, where Z is a non-dimensional rescaled vertical coordinate centered at the jet core.

An important phenomenon is that scalings of various (horizontally-averaged) turbulent quantities, typically, exhibits multi-valued, but well-defined and distinct, scaling branches (four of them). Multiple scalings exist irrespective of which scaling parameter one may choose (Ri_g , Fr_t , Re_b etc.). First, there are two distinct scaling curves corresponding to data points in the upper and lower flanks of the jet. These curves are precisely delineated at the level of minimum shear in the quasi-equilibrium turbulent mean velocity profile (which occurs at $Z \approx 0.09$ in the control simulation dataset). The scaling curves, on each side of the jet, also undergo a branch switching. It has been found, after examining several plausible candidates (N^2 , outer length scale cross-overs etc.), that branch switching is best delineated at the inflection point (hereafter denoted as IP) levels of the quasi-equilibrium turbulent mean jet velocity profile (which occurs at $Z \approx 1.3$ and $Z \approx -1.4$ in the present dataset, cf. Fig. 3a). The inner core region, inward of the IP levels, will be referred to as the *inner* scaling region (denoted by open symbols in all scaling figures to follow). The region outside of the IP levels are called the *outer* scaling region (denoted with filled symbols in figures).

2.4 Length scales, ratios and flow regimes

A need for new methods of investigating turbulence, utilizing measurements of energy-containing (outer) scales of turbulence, which are more easier to measure than dissipation scales, had been widely recognized. Small (outer) vertical scales ($O(1 \text{ m}-100 \text{ m})$), in the lower stratosphere, controlling the size of "sheets" and turbulent "layers", are also evident from high-resolution temperature measurements (Alisse and Sidi 2000; Luce et al. 2002). The main dynamical properties of such layers, whether strongly mixed or not, can be characterized not only by Ri_g , but also by various other outer scale ratios. Hence, it is of great interest to examine the vertical variability of shear stratified turbulence outer scales, and the scalings of some important outer length scale ratios, with Ri_g , using the present high resolution numerical dataset. Through this approach, we also obtain a conceptual model of inhomogeneous flow regimes and transitions (in the vertical) expected of a turbulent tropopause jet.

Vertical profiles of various normalized length scales and some of their ratios, for the control simulation, are presented in Fig. 4a and Fig. 4b, respectively (cf. section 2.7 for definitions). One can notice that the dissipation scale (L_d) is of the same order as the Ozmidov scale (L_o) (or the buoyancy scale (L_b)) within the turbulent core (i.e. turbulence is only marginally affected by stratification). The cross-over of L_o (or L_b) and L_d occurs at $Z \approx 2.1$ (upper

half), and $Z \approx -3.0$ (lower half), which indicates the onset of buoyancy influences. One might call the region $0.2 < Z < 2.1$ as a *shear-dominated* regime, and the region $Z > 2.1$ as a *buoyancy-affected* one. However, in terms of scalings, noted in previous section, branch switchings occur at the *IP* levels (say, $Z \approx 1.3$). Therefore, the zone $1.3 < Z < 2.1$ inherits the scaling characteristics of the buoyancy-affected regime, and so is also influenced by stratification effects. Note that the region $-0.2 < Z < 0.2$ has been excluded from the discussion above because the Tatarski scale (L_t) and the Ellison scale (L_e) cross-over there, and the TKE balance is mainly between the transport term and the dissipation in this narrow layer. One may thus reasonably expect an inertial range, unaffected by anisotropic shear or stratification effects, in this innermost narrow layer. In the following discussion, we consider further regime transitions only in the upper flank of the jet, after noting that the overall effect of asymmetric stratification is to delay the onset of various transitions by a small vertical distance in the lower flank of the jet. The cross-over between L_t and L_e occurs at $Z \approx 3.6$, which indicates that extraction of energy from mean shear is not efficient above this level. The scales L_o (or L_b) and L_t (or the shear scale, L_s) also cross-over in the near vicinity ($Z \approx 3.8$). It may also be noted, from Fig. 3d, that this cross-over level corresponds well with the critical value of $Ri_g \approx 0.25$. One could thus identify this as a transition from the buoyancy-affected regime to a *buoyancy-dominated* regime. It is also interesting to note that L_d/L_e remains nearly a constant over the range $-6 < Z < 6$ (cf. Fig. 4b), which suggests that these scales can be used as surrogates in practical applications. Thus, it may be summarized that, as one traverses away from the innermost jet core, the following sequence of regime transitions are encountered: shear-dominated \rightarrow buoyancy-affected \rightarrow buoyancy-dominated. It is also important to recall that the scaling characteristics of the buoyancy-affected regime, however, extends into the shear-dominated regime up to the IP levels. Thus, a purely shear-dominated zone (unaffected by buoyancy influences) is, in fact, confined to the layer $0.2 < Z < 1.3$ (on the upper jet-flank).

In Fig. 5, scalings of some length scales/ratios with Ri_g are shown. The increasing trend in the scaling of L_t (normalized), an outer scale of specific interest to OT studies, with Ri_g , shown in Fig. 5a, is in agreement with radar estimates of that quantity near the tropopause (cf. Eaton and Nastrom 1998).

2.5 Mixing efficiency and eddy mixing coefficients

Incomplete understanding of turbulent mixing processes in stably stratified boundary layers or the stable free atmosphere is well-known (Kim and Mahrt 1992; Mahrt 1998). Recent analysis of radiosonde profiles, for a 10-year period, indicates the presence of a thin, strongly stratified layer near the tropopause, which is not evident in large-scale atmospheric model outputs, partially due to the coarse vertical resolution employed in those models (Birner et al. 2002). It is clear that existence of such a layer could have important implications, especially for the stratosphere-troposphere exchange processes. One may argue that a proper representation of vertical mixing processes associated with the shear instability of zonal jets will be crucial for achieving a sufficiently sharp tropopause as seen in the

observations. With such applications in mind, we also evaluate the performance of some commonly used Ri_g -dependent formulae for the eddy diffusivities of momentum and heat using the present numerical dataset.

Flux Richardson number (Ri_f ; also called mixing efficiency) and turbulent Prandtl number (Pr_t) are crucial parameters in simple first-order turbulent mixing schemes (cf. Kim and Mahrt 1992; Schumann and Gerz 1995; Pardyjak et al. 2002). They are defined as: $Ri_f = -BP/SP$ (cf. section 2.7 for SP and BP definitions), and $Pr_t = Ri_g/Ri_f = K_m/K_h$, when the momentum and heat fluxes are downgradient. Here K_m and K_h are the eddy viscosity and eddy diffusivity coefficients, respectively, defined as: $K_m = SP/S^2$ and $K_h = -\langle \theta' w' \rangle / (\bar{d}\theta/dz)$. Traditionally, many geophysical applications assumed that mixing efficiency (Ri_f) is a constant (≈ 0.2), in which case Pr_t grows linearly with Ri_g . However, there is now accumulating evidence, from numerical simulations and field observations, which suggests that mixing efficiency is a highly variable quantity (cf. Kennedy and Shapiro 1980; Kim and Mahrt 1992; Bertin et al. 1997; Smyth et al. 2001; Pardyjak et al. 2002). Several atmospheric or oceanic models utilize simplified (unique) relationships between Ri_f (or Pr_t or K_m or K_h) and Ri_g in their subgrid-scale turbulent mixing parameterization schemes (cf. Pacanowski and Philander 1981; Peters et al. 1988; Kim and Mahrt 1992; Tjernström 1993; Wilson 2002; Pardyjak et al. 2002).

The scalings of Ri_f , Pr_t , K_m , and K_h , with respect to Ri_g , in the present simulation data is presented in Fig. 6, where K_m and K_h are normalized. In these scalings, we restrict discussion to the region for which vertical fluxes are downgradient; i.e. $BP < 0$ (since $d\bar{\theta}/dz > 0$ everywhere along the profile) and $SP > 0$.

It is of interest to examine whether some simple Ri_g -dependent parameterization formulae for K_m , K_h , and Pr_t (popular among atmospheric/oceanic numerical modeling community) can, at least, qualitatively reproduce the shape of the scalings obtained in our simulation data. For this purpose, in Fig. 7, we consider, for brevity, only the (upper) outer scaling branches. The models used in this comparison are: *linear* (cf. Kim and Mahrt 1992), *T93* (Tjernström 1993), *SG* (Schumann and Gerz 1995), *PP* (Pacanowski and Philander 1981), *MPI* (Max Plank Institute scheme) suggested in Latif et al. 1994 (cf. Wilson 2002), and *L81* (Louis et al. 1981). The *L81* model follows from models for turbulent mixing lengths of momentum ($l_m = (K_m/|S|)^{1/2}$) and heat flux ($l_h = (K_h/|S|)^{1/2}$), where $l_m^2 = l_{0,m}^2 [1 + 10Ri_g(1 + 5Ri_g)^{-1/2}]^{-1}$ and $l_h^2 = l_{0,h}^2 [1 + 15Ri_g(1 + 5Ri_g)^{1/2}]^{-1}$ (with our fitting constants $l_{0,m}^2 = 0.299$ and $l_{0,h}^2 = 0.522$) (cf. Kim and Mahrt 1992; Tjernström 1993). Then, the Pr_t model (*L81*) is obtained from the definition: $Pr_t = K_m/K_h$. From Fig. 7a, it is clear that, for Pr_t , *T93* model is the one in best agreement with our dataset. The *PP* model fits best the shape of outer scaling for K_m (Fig. 7b). None of the three models of K_h appears satisfactory (Fig. 4c). However, if one combines K_m model of *PP* and Pr_t model of *T93*, a better model for K_h can be obtained through the relation $K_h = K_m/Pr_t$. This curve is denoted in Fig. 7c as *PP + T93*. Clearly, more research is needed, especially for the lower stratosphere.

2.6 Eddy mixing in jet-stream turbulence under stronger stratification

Certain qualitative changes in turbulent eddy mixing during transitional regimes towards stronger stratification are highlighted using high-resolution numerical simulations. The behavior of turbulent eddy mixing parameters found in this study is consistent with some recent observational results in stably stratified shear flows in the atmosphere. In particular, the flux Richardson number increases, saturates and then decreases after a critical value of the gradient Richardson number (Ri_g) around 2.0. Correspondingly, there is also a transition from a decreasing trend in the turbulent eddy mixing coefficient for momentum to an increasing one at the same critical Ri_g . The implication of the study is that such a transition can be of quite general interest in sheared flows under stronger stratification (with significant wave dynamics), and needs to be accounted for in the parameterization of microscale atmospheric turbulence.

The possibility that eddy mixing coefficient of momentum (K_m) might increase with the gradient Richardson number (Ri_g) has recently been pointed out through observations in stably stratified, katabatic atmospheric boundary flows (Monti et al. 2002; hereafter M02), and also stably stratified shear flows in laboratory experiments (Strang and Fernando 2001; hereafter SF01). This result is somewhat counter-intuitive to the common wisdom that turbulent mixing will be stronger as Ri_g decreases below the critical Ri_g about 1/4 predicted by the linear theory, through the onset of Kelvin-Helmholtz (KH) type shear instabilities. However, as pointed out by SF01, a transitional regime from KH dominated regime to wave instabilities (i.e. growing Hölmboe and/or internal waves) can occur when Ri_g is O(1). Under strongly stably stratified conditions, dominated by wave-like motions, countergradient heat fluxes and production of turbulent motions by the buoyancy term in the kinetic energy budget are rather typical (Komori et al. 1983; Einaudi and Finnigan 1993).

The generality of the transitional scaling behavior for K_m , reported in SF01 and M02, is yet to be established. To our understanding, so far no numerical simulations have reproduced such a scaling. The main contribution of the present work is to demonstrate the possibility of K_m increasing with Ri_g in datasets obtained through high resolution numerical simulations in the context of shear stratified turbulence in a nonuniformly stratified tropopause jet. The reliability of the dataset (and hence that of the present result) is confirmed by the quasi-balanced nature of the budgets of turbulent kinetic energy and vertical fluxes (see subsection 2.6.3). It is expected that the present study might thus provide valuable information in interpreting transitional flow behavior in a variety of atmospheric flows under relatively stronger stratification in comparison to shear.

High-resolution numerical simulations of jet-stream generated turbulence (at vertical scales on the order of 1m - 10 m), with nonhomogeneous vertical profiles of mean shear and stratification, have been the focus of our previous studies using the fully nonlinear, three-dimensional (3D), incompressible, stratified Navier-Stokes equations, under the Boussinesq approximation (Tse et al. 2003; Joseph et al. 2003 and 2004). The existence of

multi-valued branches in the scalings of various turbulent quantities against Ri_g has been demonstrated in Joseph et al. (2004) (hereafter JMNT). Such branches originate from points of minimum gradient Richardson number along the flanks of the jet. The only major difference between that study and the present one is that Brunt-Väisälä (or buoyancy) frequency ($N = ((g/\Theta_0)\partial\Theta/\partial z)^{1/2}$) is increased by a factor of 3 in the latter. The vertical fluxes of momentum and heat in the present configuration are still downgradient. But the signature of a clear transition in the scaling of the turbulent eddy mixing coefficient of momentum becomes evident in the case of stronger stratification. At such a transition around $Ri_g \approx 2$ (Figure 11a), a saturation of the flux Richardson number Ri_f also occurs along the scaling branch corresponding to the most stably stratified upper flank of the jet. After this saturation, Ri_f shows a tendency to decrease.

2.6.1 Model and Simulation

The Boussinesq model and simulation methodology used in the present study is exactly the same as those described in JMNT, and hence are not repeated here. Essentially, the model equations are forced by horizontally homogeneous momentum and thermal source terms (but partially balanced by basic state viscous terms) that maintain a background (synoptic-scale) jet-stream and the doubling of N across a model tropopause throughout the simulation. The simulation is continued until quasi-balanced budgets for turbulent velocity variances and fluxes (i.e. a quasi-equilibrium) have been obtained. In the parameter set-up of the present simulation, the only differences from JMNT are in the stratification parameter $N = 0.6$, and the kinematic viscosity, $\nu = 0.0005$ (instead of 0.2 and 0.0001, respectively for N and ν , used in JMNT). The numerical simulation has a resolution $128 \times 128 \times 1024$, in a normalized computational domain: $x[0, \pi/2]$, $y[0, \pi/2]$, and $z[-5.5, 5.5]$. The domain is centered at the jet maximum located at $z = 0$, and is periodic in the horizontal direction. The rescaled vertical coordinate is $Z = z\alpha$, where α is a stiffness parameter in the Gaussian-type function used for the momentum source. The robustness of the results presented in this paper has been verified at two vertical resolutions (512 and 1024 levels). The scaling curves in Figures 11 and 12 are found to be identical with doubled numerical resolution.

The vertical profiles of turbulent mean streamwise velocity (U) and total mean potential temperature (Θ), Brunt-Väisälä (or buoyancy) frequency (N), vertical shear of the mean horizontal velocity ($S = ((\partial U/\partial z)^2 + (\partial V/\partial z)^2)^{1/2}$), and $Ri_g = N^2/S^2$) at the quasi-equilibrium stage of the numerical simulation are presented in Figure 8a-8c, respectively. The corresponding turbulent variances and vertical momentum and heat fluxes are given in Figure 9. One significant feature that deserve attention is the N^2 -bulge near the centre of the jet (Figure 8b), which is an effect of stronger stratification (cf. JMNT). This results in a secondary peak for the fluctuating temperature variance (through the gradient production) near the center of the jet (cf. Figure 9a). Within the core of the jet, on either sides, Ri_g is less than 1/4, thus conducive for shear instabilities. The present simulation has a range of Ri_g which lies within atmospheric measurements (cf. M02). Examining Figures 8a and

9b, it is clear that the fluxes, $\langle u'w' \rangle$ and $\langle \theta'w' \rangle$, are down-gradient. In this paper, an angle bracket $\langle \cdot \rangle$ always denote a horizontal average (because of horizontal homogeneity in the background flow configuration).

The budgets of $q^2 = \langle u'^2 + v'^2 + w'^2 \rangle$, which is proportional to the turbulent kinetic energy (TKE), the momentum flux $\langle u'w' \rangle$ and the heat flux $\langle \theta'w' \rangle$, for the present horizontally homogeneous case, are given in Figure 10a-c. The notations in the figure denote shear production (SP), buoyancy (B), dissipation (D), vertically-redistributive transport (TR ; including contributions from triple moment, pressure, and dissipation), and the gradient production (GP) terms. Interested reader may refer to their expressions in JMNT. The buoyancy contribution in the TKE budget had been negligible in the strongly sheared case (cf. JMNT), while it becomes significant in the present simulation under stronger stratification. We have also splitted the vertical transport terms in these budgets in order examine the relative strengths of contributing terms (figures not shown for the sake of brevity); the main results are summarized below. In the TKE vertical transport term, pressure contribution is the largest, corresponding to a gain near the centre and a loss on either sides of the jet. The triple-moment transport is interestingly nearly out-of-phase with the pressure transport, in agreement with strongly sheared case examined in JMNT. In the $\langle u'w' \rangle$ budget pressure and triple moment transport terms are of comparable magnitude, and show nearly in-phase relationships. However, in the budget of $\langle \theta'w' \rangle$, pressure contribution is the single dominating one and the triple-moment contribution is much smaller. In all the three budgets, the dissipative contributions to the vertical redistribution (transport) are negligible.

The scalings of turbulent eddy mixing parameters, the flux Richardson number $Ri_f = B/SP$, the turbulent Prandtl number ($Pr_t = Ri_g/Ri_f = K_m/K_h$), and the eddy mixing coefficients of momentum ($K_m = [\langle u'w' \rangle(\partial U/\partial z) + \langle v'w' \rangle(\partial V/\partial z)]/S^2$ and heat ($K_h = -\langle \theta'w' \rangle/(d\bar{\theta}/dz)$)) are presented in Figure 11. The turbulent eddy mixing coefficients are normalized by U_o/α , where U_o is the mean jet-centerline velocity. Multi-branched nature of scalings are in qualitative agreement with results of JMNT. It has been found that the inflection point (hereafter denoted as IP) criterion, proposed in JMNT, is successful in delineating the branch switching between different scaling branches. The IP levels in the mean velocity profile are approximately at ± 1.15 in the present dataset and correspond to minima of Ri_g , which are smaller than 0.25 (Figure 10c). The inner core region, inward of the IP levels, will be referred to as the *inner* scaling region (denoted by open symbols in Figure 11). The region outside of the IP levels are called the *outer* scaling region (denoted with filled symbols in Figure 11).

One important aspect we wish to emphasize in this paper is the saturation of Ri_f (Figure 11a) and a transition in the scaling behavior of K_m (Figure 11c), both of which occur at $Ri_g \approx 2$, along the most stably stratified outer scaling branch in the upper flank of the jet. After this transition, Ri_f shows a tendency to decrease and K_m shows a tendency to increase as a function of Ri_g . This finding is in qualitative agreement with observational results for stably stratified nocturnal boundary layer flows (cf. M02 and Pardyjak et al. 2002) and shear-stratified flows in laboratory experiments (cf. SF01). From Figure 11b, a similar transition along the outer scaling branch for the turbulent Prandtl number Pr_t

occurs around $Ri_g \approx 2$ with $Pr_t \approx 1$ before the transition, and a sharp increase up to $Pr_t \approx 10$ after the transition. Similar transitions for Pr_t have been observed in stably stratified atmospheric boundary layers by Kondo et al. (1977) and Gossard and Frisch (1987) with the same range of Pr_t^{-1} between 1 and 0.1, with a sharp decrease around $Ri_g \approx 1$.

In Figure 12, a more appropriate non-dimensionalization of K_m and K_h , rescaled by $\langle w'^2 \rangle / S$, suggested in M02 also yields similar features with transition at $Ri_g \approx 2$. The rescaled eddy coefficients are denoted by a prime in this figure. As proposed in M02, it is likely that increasing influence of buoyancy, for $Ri_g > O(1)$, accentuate internal gravity wave activity, which sustains transport of momentum, but not much of the heat fluxes. This is indicated by the faster decrease of K'_h , compared with K'_m , with increasing Ri_g (cf. Figure 12). The importance of wave-turbulence interactions resulting in significant coupling between different vertical levels, through nonlocal transport terms, is being recognized through observational studies in the stable atmospheric boundary layer (Einaudi and Finnigan 1993; Finnigan 1999). We have also examined the budgets of turbulent vertical fluxes of momentum ($\langle u'w' \rangle$) and heat ($\langle \theta'w' \rangle$) (not shown). The contributions through pressure transport and triple moment transport are indeed large in the budgets, indicating significant vertical coupling through wave-turbulence interactions. Some preliminary simulations have been done with a broader (by a factor of two) jet. The inflection point (IP) criterion is very robust, with branches of scaling curves (Figure 11) originating from the very same minimum $Ri_g \approx 3.0 \times 10^{-2}$, albeit the vertical IP levels of the broader jet are different; the scaling curves in Figures 11 and 12 are similar.

The whole scenario also bears some correspondence with the linear stability analysis by Lott et al. (1992) of a shear layer, with an N^2 -notch, which demonstrates the coexistence of propagating wave modes in addition to Kelvin-Helmholtz modes (see also, Davies and Peltier 1978). The scaling transition along the outer branch appears consistent with the expectation of propagating wave instabilities identified by Lott et al. (1992) outside of the N^2 notch in the more stably stratified regions.

An important point in this study concerns the increase of K_m with Ri_g (for $Ri_g > 2$) noticed in Figure 11c, which is in qualitative agreement with the results from stably-stratified nocturnal katabatic flows (M02, Pardyjak et al. 2002). As pointed out in the latter study, the dominating role of internal wave instabilities is attributed as the cause for this seemingly anomalous scaling behavior in our simulation data too. Correspondingly, the flux Richardson number increases, saturates and then decreases after a critical value of the gradient Richardson number (Ri_g) around 2.0. The implication of the present study is that such a transition arising out of wave-turbulence interactions can be of quite general interest in sheared flows under stronger stratification (with significant wave dynamics), and needs to be accounted for in the parameterization of microscale atmospheric turbulence in mesoscale meteorological models.

2.7 Outer length scales of turbulence and parameters critical for ABL C_n^2 parameterizations

Here, definitions of some outer length scales, and scaling parameters relevant to stably stratified, shear flows are briefly provided. We first introduce the following notations:

$$\begin{aligned} q^2 &= \langle u'^2 + v'^2 + w'^2 \rangle, \\ \epsilon &= \nu \langle (u'_{,j})^2 + (v'_{,j})^2 + (w'_{,j})^2 \rangle, \\ S^2 &= (\partial \langle U \rangle / \partial z)^2 + (\partial \langle V \rangle / \partial z)^2, \\ SP &= -\langle u'w' \rangle d\langle U \rangle / dz - \langle v'w' \rangle d\langle V \rangle / dz, \\ BP &= N_o \langle w'\theta' \rangle, \\ TR &= \frac{1}{2} \frac{\partial}{\partial z} [\nu \frac{\partial}{\partial z} \langle q'^2 \rangle - \langle w'q'^2 \rangle - 2\langle p'w' \rangle]. \end{aligned}$$

where the subscript $,j$ in expression for ϵ denotes $\partial/\partial x_j$ for $j = 1, 2, 3$ and $\{x_j\} = (x, y, z)$. The above quantities are, respectively, the turbulent velocity variance (q^2) and the TKE dissipation rate (ϵ), squared mean shear (S^2), the shear production (SP), the buoyancy sink/source (BP), and the TKE transport term (TR). Well within the viscous dissipation range, is the Kolmogorov microscale, $L_k = (\nu^3/\epsilon)^{1/4}$, which is the smallest turbulent length scale at which viscous forces are of the same magnitude as inertial forces. The definition of an outer scale for turbulence (L_{out}) is not unique, and there are various candidates depending on the relative magnitudes of shear, buoyancy, and inertial influences (cf. Hopfinger 1987; Hunt et al. 1988; Rohr et al. 1988; Phillips 1991; Moum 1996; Smyth and Moum 2000; Fernando 2002).

A macroscale for turbulent motion is the *dissipation scale* defined as $L_d = q^3/\epsilon$. The loss of energy from these scales occurs through nonlinear energy cascades. A balance between inertia and buoyancy forces can either result in *Ozmidov* (also called *Dougherty*) *scale*, defined as: $L_o = (\epsilon/N^3)^{1/2}$, or the *buoyancy scale*, defined as $L_b = q/N$ (Dougherty 1961; Ozmidov 1965; Hunt et al. 1988). The former is an upper limit on inertial-range turbulent motions in a stably stratified fluid and the latter involves contributions both from turbulence and waves, and is more directly related to the motion of a parcel. The scale $L_{bw} = \sigma_w/N$ approximates the largest distance a parcel will be displaced against gravity if all of its kinetic energy, in the vertical motion, were converted to potential energy, and it signifies the onset of buoyancy effects (cf. Fernando 2002). For sheared flows, there are two analogous scales, at which eddies are deformed by shear, called the *Tatarski* (also called *Corrsin*) *scale*, defined as $L_t = (\epsilon/S^3)^{1/2}$, and the *shear scale*, $L_s = q/S$ (Corrsin 1957; Tatarski 1961; Eaton and Nastrom 1998; Fernando 2002). It may also be noted that $L_b^3 = L_o^2 L_d$ and $L_t^2 = L_s^3 / L_d$. An overturning scale is the *Ellison scale* (cf. Ellison 1957), defined as $L_e = \sigma_{\theta'}/(\bar{d}\theta/dz)$, where $\bar{\theta} = \Theta_o + \langle \theta \rangle$, and $d\bar{\theta}/dz = N_o K^2 + \partial \langle \theta \rangle / \partial z$. The scale L_e represents a typical vertical distance traveled by fluid parcels before either mixing with its new surroundings or returning towards their equilibrium levels.

The *gradient Richardson number*, given by $Ri_g = N^2/S^2$, is related to some length scale ratios as: $Ri_g = (L_t/L_o)^{4/3} = (L_s/L_b)^2 = (L_d^{2/3} L_t^{4/3})/L_b^2 = L_s^2/(L_d^{2/3} L_o^{4/3})$. Similarly,

the *turbulent Froude number* (Fr_t) is defined here as $Fr_t = \epsilon/(Nq^2)$ is related by $Fr_t = L_b/L_d = (L_o/L_d)^{2/3} = (L_o/L_b)^2$. Considering L_d as the relevant macroscale, a *turbulent Reynolds number* is defined as: $Re_t = qL_d/\nu = q^4/(\nu\epsilon) = (L_d/L_k)^{4/3}$. A *buoyancy Reynolds number*, which measures the strength of turbulence in relation to buoyancy forces, is given by $Re_b = \epsilon/(\nu N^2) = (L_o/L_k)^{4/3}$. It may be noted that the ratio (L_o/L_k) is a measure of the range over which a locally isotropic, inertial-range is valid in stratified turbulence (Phillips 1991). A *turbulent shear number* can be defined as: $Sh_t = Sq^2/\epsilon = (L_d/L_t)^{2/3} = (L_s/L_t)^2 = L_d/L_s$. When $Sh_t \gg 1$, turbulence is effectively strained by shear and extracts energy from it (cf. Fernando 2002). Analogous to Re_b , one may also define a *shear Reynolds number* as (cf. Corrsin 1957; Smyth and Moum 2000): $Re_s = \epsilon/(\nu S^2) = (L_t/L_k)^{4/3}$. It may also be noted that $Ri_g = Re_s/Re_b$.

For convenience, definitions of various length scales and parameters utilized in the present study are summarized in Tables A1-A2.

Table A1. Turbulence outer length scales: definitions

L_k	L_d	L_o	L_b	L_t	L_s	L_e
$(\nu^3/\epsilon)^{1/4}$	q^3/ϵ	$(\epsilon/N^3)^{1/2}$	q/N	$(\epsilon/S^3)^{1/2}$	q/S	$\sigma_{\theta'}/(d\theta/dz)$

Table A2. Nondimensional Parameters: definitions

Ri_g	Fr_t	Re_t	Re_b	Sh_t	Re_s
$(L_t/L_o)^{4/3}$	$(L_o/L_b)^2$	$(L_d/L_k)^{4/3}$	$(L_o/L_k)^{4/3}$	L_d/L_s	$(L_t/L_k)^{4/3}$

Table 1. Outer scaling power laws:
statistics versus Ri_g

	$\langle w' ^2 \rangle$	$\langle \theta' ^2 \rangle$	$\langle u'w' \rangle$	$\langle \theta'w' \rangle$
$Ri_g < 0.25$	-0.33	0.33	-0.50	-0.20
$Ri_g > 0.25$	-0.20	0.17	-0.33	-0.25

Table 2. Outer scaling power laws:
length scales/ratios versus Ri_g

	L_t	L_e/L_o	L_e/L_b	L_s/L_o	L_e/L_{sw}	L_{sw}/L_{dw}
$Ri_g < 0.25$	0.33	0.25	0.13	0.67	-0.33	0.20
$Ri_g > 0.25$	0.67	0.17	0.11	0.60	-0.33	0.33

Table 3. Outer scaling power laws:
scaling parameters versus Ri_g

	Sh_t	Fr_t	Re_b	Re_t	Re_s
$Ri_g < 0.25$	-0.25	-0.20	-0.67	-0.25	0.33
$Ri_g > 0.25$	-0.33	-0.11	-0.33	-0.11	0.67

Table 4. Outer scaling power laws (upper jet-flank):
mixing parameters/coefficients versus Ri_g

	Ri_f	Pr_t	K_m	K_h
$Ri_g < 0.25$	0.50	0.50	-0.25	-0.75
$Ri_g > 0.25$	0.50	0.50	0.00	-0.50

Table 5. Outer scaling power laws (lower jet-flank):
mixing parameters/coefficients versus Ri_g

	Ri_f	Pr_t	K_m	K_h
$Ri_g < 0.25$	0.75	0.25	-0.25	-0.50
$Ri_g > 0.25$	0.75	0.25	0.00	-0.25

Table 6. Models for mixing parameters/coefficients. Models for l_m^2 and l_h^2 are defined in the text (cf. section e). Abbreviations defined in caption to Fig. 7 (see also section e).

Models	K_m	K_h	Pr_t
<i>linear</i>	-	-	$a_0 + a_1 Ri_g$; ($a_0 = 0.868, a_1 = 1.922$)
<i>T93</i>	-	-	$(a_0 + a_1 Ri_g)^{1/2}$; ($a_0 = 0.162, a_1 = 20.1$)
<i>SG</i>	-	-	$a_0 \exp(-Ri_g/(a_0 * 0.25)) + Ri_g/0.25$ ($a_0 = 0.74$)
<i>PP</i>	$a_0/((1 + 5Ri_g)^2) + a_1$ ($a_0 = 0.057, a_1 = 0.032$)	$a_0/((1 + 5Ri_g)^2)$ ($a_0 = 0.185$)	- -
<i>MPI</i>	$a_0/(1 + (5Ri_g)^2) + a_1$ ($a_0 = 0.056, a_1 = 0.027$)	$a_0/(1 + (5Ri_g)^2)$ ($a_0 = 0.161$)	- -
<i>L81</i>	$l_m^2 S $	$l_h^2 S $	l_m^2 / l_h^2

3 Technical Report: Stratospheric CAT

Stratospheric turbulence (altitudes 10-30 km) is an atmospheric phenomenon that has a significant impact on DoD operations. In particular, mechanical turbulence (i.e. patchy high frequency fluctuations in the stratospheric wind fields and long-lived energetic vortex structures with several hundred meters scale) impacts high altitude observing platforms. Stratospheric mechanical or clear air turbulence (CAT) is a major problem for U-2 reconnaissance aircraft as well as the newest generation of Unmanned Air Vehicles (UAV) such as the Global Hawk, Predator-B, and the High Altitude Airship (HAA). Flying through

strong stratospheric CAT causes the autopilot to begin pitch oscillations that seriously degrade photographic and synthetic aperture radar performance as well as put the platform itself at risk.

In the stratosphere Clear Air Turbulence events are associated with wave propagation, specifically long period inertio-gravity waves. All of the observations using instrumented aircraft or balloons (Barat 1975, Cot and Barat 1986, Vernin et al. 1995, Beland et al 1993, Alisse et al 2000) as well as VHF-UHF radars (Sato and Woodman 1982; Dalaudier, Sidi, Crochet, Vernin 1994, Luce et al 2002; Eaton and Nastrom 1998, 2001; Bertin et al 1997, 1999; Pavelin et al 2001, 2002) give evidence in the stratosphere of a proliferation of thin and isolated turbulent layers. The observational studies yield a wealth of information on the amplitude saturation of gravity waves in the stratosphere and support the contention that long period waves saturate through shear instability. Indeed, one of the major mechanisms explaining wave saturation is related to turbulence dissipation via shear instabilities (lateral shear). Gravity waves sources are varied: mountain waves, convective instabilities (storms) generation, highly curved and dynamically evolving jetstreams; the latter have been observed in the lower stratosphere by Pavelin et al 2001 suggesting that geostrophic adjustment is a likely source mechanism for gravity wave activity in the stratosphere. From radio soundings measurements of fronts and storm tracks Plougonven et al. (2003a, 2003b) further demonstrate that the jet region is the dominant source of gravity waves in regions far from orography; the vicinity of the maximum jet velocity and the regions of strong curvature of the jet are associated with intense gravity wave activity with generation of large amplitude inertia gravity waves propagating into the stratosphere.

From balloon sounding and SCIDAR data (stars scintillation, detection and ranging measurements) Vernin et al 1995 evidence that localized hydrodynamic instabilities engendered by the propagation of gravity and mountain waves lead to the formation of thin turbulent layers in the stratosphere, where strong stable stratification conditions prevail. They measured a Richardson number Ri_g generally smaller than one within each such thin layer (and often less than 0.25) and rapidly increasing on the edges of such layers; at the edges they observed very sharply localized peaks of C_T^2 . The layers have vertical thickness of a few hundred meters in the stratosphere above 15,000m; for instance, a layer 500m thin was measured between 19,200m and 20,000m (Figure 8 in Vernin et al. 1995). They show that vertical modulation of the horizontal wind field is generated by gravity waves propagating vertically upwards; they compute hodograph plots of the horizontal wind field after subtracting the mean wind field at every altitude and obtain closed clockwise (nearly elliptic) curves with increasing altitudes in the northern hemisphere and anti-clockwise in the southern hemisphere. They obtain nearly ellipsoidal loops vertically stacked above each other from the tropopause up to 25,000m. These near-ellipses, which reflect the saturated wave polarization, have parameters significantly changing at different altitudes in the stratosphere, reflecting nonlinear saturation dynamics and exchange of energy with the turbulent layers. Vernin et al 1995 study confirms earlier findings of Cot and Barat, 1986 and outlines several important results:

- CAT is related to a long-period wave via shear instability;

- lateral directional shear generated by wind perturbations to the mean flow triggered by gravity waves is the key instability mechanism for stratospheric CAT;
- gravity waves of long period and of short vertical wavelength can propagate upward over several wavelengths close to shear instability condition;
- turbulent layers have a thickness substantially smaller than the waves vertical wavelength ($\equiv 0.8km$);
- turbulent layers horizontal extension is of the order of the horizontal wavelength ($\equiv 10km$);
- low-frequency wave interacting with turbulence may propagate upward with an amplitude saturation so that it remains near the instability condition;
- lateral shear instability of long period waves is the mechanism for generation of thin stratospheric CAT layers.

UHF-VHF radar measurements and GPS radiosoundings by Worthington and Thomas (1997) and Bertin et al. (1999) further confirm that stratospheric CAT is systematically observed in regions of wave-induced windshears in synergy with saturated inertio-gravity wave field. They attribute this to Kelvin-Helmholtz instabilities generated by locally strong lateral windshears and point to this as the main mechanism of formation of thin layers of stratospheric anisotropic CAT.

In a recent campaign of measurements in 2002 co-sponsored by AirForce Research Laboratories and AFOSR, Vernin et al 2003, 2004 further validate gravity wave/turbulence interaction models in the lower stratosphere. This campaign has relied on both instrumented balloons (equipped with microthermal sensors) and the Generalized Scidar (GS). The latter is based on the analysis of scintillations of a double star giving continuous measurements of $C_n^2(h, t)$ for altitudes $0 < h < 25,000m$; this instrument also gives access to the fluctuating turbulent wind profile within each thin turbulent layer. They extract propagating gravity wave parameters at different altitudes. Their technique is based on selecting a portion of the atmosphere where the oscillation of velocity (after removing the mean) are well characterized; computing the vertical wavenumber component after bandwidth filtering of the local vertical wavelength; computing the local horizontal wavenumbers through ellipse fitting in the hodograph plane of horizontal velocity fluctuations. They obtain a catalogue of gravity wave parameters including the wavenumber inclination with respect to the horizontal plane at different altitudes from $13,700m$ all the way up to $25,900m$. Vernin et al (2003, 2004) demonstrate the impact of weak rotation on the observed gravity wave dynamics; the thin CAT layers are often long lived, upto and beyond 8 hours, and therefore they do incorporate rotation parameters in their polarization relations for gravity wave dynamics (Vernin, private communication). Their findings on the impact of weak rotation on strongly stratified stratospheric flows corroborate the earlier theoretical findings of Babin, Mahalov and Nicolaenko (1997, 1998, 2002) based on the strong nonlinear theory of wave-potential vorticity interactions in the regimes of large Burger number (strong stratification,

weak rotation regime). Vernin et al (2003, 2004) measure many thin turbulent CAT layers with Richardson number Ri_g smaller than 0.25 within each layer. Each layer corresponds to peaks in the vertical gradient of the horizontal wind speed as the result of the horizontal wind shear. This shearing process is produced by a gravity wave activity and is associated with a large gradient of potential temperature. Around the 20,000m level layer thickness ranges from 200m to 500m. This presents a serious challenge to the High Altitude Airship (HAA). The vertical velocity fluctuations reach 5m/s for the stratospheric CAT at altitudes around 20,000m. Encountering such strong CAT layers causes the autopilot of Unmanned Air Vehicles (UAV) such as the Global Hawk, Predator-B and the High Altitude Airship to begin pitch oscillations that seriously degrade photographic and synthetic aperture radar performance as well as put the platform itself at risk. Stratospheric flying UAVs such as the Global Hawk are even more highly susceptible to CAT since the controller on the ground may not recognize they are in a potentially dangerous situation until it is too late.

We have performed high resolution 3D numerical simulations on massively parallel architectures using our anelastic microscale code (with adaptive nonuniform vertical gridding) to resolve and extract the microscale physics of such long-lived thin CAT layers. Adaptive vertical gridding based on adaptive domain decomposition enables us to resolve scales down to 1m in a CAT layer while considerably relaxing the vertical gridding in subdomains characterized by relatively calm dynamics. The initialization of our microscale codes is based on both WRF/MM5 mesoscale input (mean velocity and temperature profiles) and the catalogues of polarized wave velocity fluctuations (gravity waves dynamics) obtained in the AFRL/AFOSR sponsored campaigns such as Vernin et al 2003 and the one planned for Fall 2004; potential temperature fluctuations will also be inputted.

With initialization based on Cot and Barat 1986 data, we have performed such simulations and benchmarked our results against available field observations.

We have found that:

- Stratospheric CAT is related to shear instability associated with gravity waves (lateral directional shear is the key instability mechanism);
- Stratospheric CAT layers around 20,000m altitude are dominated by strong energetic eddies with typical horizontal scale $\sim 500m$ (these eddies are not resolved in simulations with MM5 and WRF mesoscale codes);
- rms fluctuating vertical velocity in CAT layers is of the same order as the mean horizontal wind speed; strikingly, we find the same 4.5m/s range measured by Vernin et al, and our fine vertical gridding yields higher local peaks of 7 m/s for the vertical velocity fluctuations;
- Our results on the length and velocity scales of energetic eddies are consistent with observations of the CAT structure in the stratosphere reported in the literature (Cot, Barat et al.). Also, U-2 pilots indicated the time sensitivity to the temperature oscil-

lations would put the length scale in the range about 1200 to 400 meters (Cote and Jumper, VSBL AFRL Trip Report to Beale AFB);

- Such stratospheric CAT layers cannot be resolved in mesoscale meteorological codes such as MM5 and WRF.

The next figures from our simulations show the CAT layers between 19,500m and 21,000m (microscale anelastic code simulations). From Fig. 15-16 the peak R.M.S. *variance* of the vertical velocity is around 4.2m/s and is of the very same order of magnitude as the *mean* horizontal wind velocity (around 5m/s). This is in marked contrast to vertical shear-dominated turbulence around a jet stream at the tropopause, and a signature of the lateral shear turbulence within the thin stratospheric CAT layers.

Figure 14 shows the horizontal velocity field on a horizontal cross section at 20,300 meters, the core of the CAT layer.

Fig. 15 superimposes contour lines of the total potential temperature with color contours for the temperature fluctuation as well as colour contours for the vertical velocity, in a randomly chosen vertical cross-section. Strong deformations of the total potential temperature contour lines closely correlate with pockets of strongly positive or negative fluctuations as well as with patches of vertical velocity $\sim \pm 5\text{m/s}$. Vertical gradients of temperature as much as 5°K per 300-500m are observed and confirm observations of U-2 pilots.

Fig. 16, a horizontal cross-section at 20,300m, superimposes line contours of temperature fluctuations with color contours of vertical velocity w . Strong gradients of temperature are observed, pinched in between pockets of resp. (relatively) high positive w and resp. negative w . The horizontal scales of these energetic eddies range between 500m and 1000m (agreement with U-2 observations).

Fig. 17, horizontal cross-section at 20,300m, superimposes line contours of vertical vorticity with color contours of vertical velocity w . Strong “islands” of vertical vorticity are closely correlated with pockets of (relatively) high w ; this is a signature of lateral (horizontal) shear turbulence.

We are continuing our studies of 3D instabilities and turbulent dynamics of helical velocity profiles $(U(z), V(z), 0)$ embedded in vertically variable background stratification $N(z)$. The conventional $Ri_g \sim 0.25$ criteria does not hold for such flows for which lateral shear is the key instability mechanism. Such velocity profiles associated with gravity waves are typical for stratospheric flows at altitudes 15-30km. Our goal is to propose simple criteria which can be used for forecasting of stratospheric CAT from mesoscale codes via post-processing.

With the help of our 3D microscale anelastic code with high vertical adaptive resolution, our goal is to impact on the development of a real-time operational model capable of forecasting (most likely via post-processing) stratospheric CAT. Such a product would originate at AFWA, would probably be based on the new generation WRF mesoscale code and extend to at least 70,000ft. Not only is there a dearth of tropopause/stratospheric physics

in current versions of WRF, but stratospheric CAT layers are not resolved by WRF. Such layers around 20,000m altitude are dominated by thin strong energetic eddies with typical horizontal scales from 500m to 1200m . Our current simulations do predict length and velocity scales of energetic eddies remarkably consistent with observations of CAT structures reported in the literature and by U-2 pilots. Persistence of large horizontal scales and patchy fine-layered vertical structures is characteristic of stratospheric CAT. We are investigating the propagation of gravity waves of long period and short vertical wavelength close to shear instability conditions and the genesis of fine layered energetic eddies via lateral directional shear instability ; this is significantly different from conventional wave-breaking physics. We are constructing tables of multi-valued scaling curves with multiple branches for length and rms velocity scales for a catalogue of representative stratospheric field conditions; we focus on cases of CAT from dynamic sources which cannot be properly represented by current codes as the NRL MWFM (Mountain Wave Forecast Model), e.g. mountain waves breaking through a strong Jet Stream, gravity waves generated by dynamical deformations of a Jet Stream, gravity waves dynamics coupled with convection induced turbulence below the tropopause (Hunt et al 2003a, b).

We are using our DNS microscale code nested within the WRF to examine the statistics and variability of turbulence outer length scales, K_m , K_h and other turbulence parameters for shear stratified turbulence in the lower stratosphere. For a catalogue of representative atmospheric field conditions, tables are being constructed of multi-valued scaling curves with multiple branches for turbulence outer length scales with the scales expressed in terms of parameters that are easily retrieved from mesoscale codes with improved physics parameterizations. A conditional sampling strategy (based on measurable or resolved mesoscale quantities) is implemented. Statistical conditional sampling is done in Bayesian framework with the minimum Bayes risk criterion (Hoel et al. 1971). This will be useful in understanding at least a fraction of the scatter (or variability) found when field measurements are plotted against any scaling parameter. Operationally, such a catalogue of representative cases can be used as a look up table for CAT prediction for operations of DoD platforms. Tables are constructed of multi-valued scaling curves with multiple branches for length and rms velocity scales for representative stratospheric field conditions. The focus will be on CAT triggered by sources such as gravity waves generated by dynamical deformations of a jet stream, gravity waves dynamics coupled with convection-induced turbulence from below the tropopause, and mountain waves breaking through a strong jet stream.

4 Collaboration with Air Force Laboratories and the ABL Program

We have closely interacted with the ABL/ADA (Atmospheric Decision Aid) Program managed by Col. Randy Lefevre (ABL/SPO, Kirtland AFB). Our goal is to develop a microscale (finer grid) turbulence code coupled with the large mesoscale (large grid) WRF codes currently developed by the Air Force. Mesoscale Meteorological codes alone (e.g.

MM5) cannot be used for prediction of Cn^2 profiles for ABL propagation codes. The output of our microscale codes is fine vertical scale modeling of Cn^2 and development of simpler 3D slew turbulence parametrization models to predict Cn^2 .

We have benchmarked our coupled mesoscale (coarse grid input)-microscale (fine vertical gridding) codes against field measurement campaigns by the Air Force; specifically the series of atmospheric measurements done at the Vandenberg AFB, Ca, in October 2001. We are closely interacting with and exchanging data with staff at the AFRL/VSBL, Hanscom AFB, MA; this includes Dr. Bob Beland, Dr. Owen Cote, Dr. George Jumper, Dr. Frank Ruggiero and Lt. Col. John Roadcap, AFRL/VSBL. We have initiated a close cooperation with AFRL/VSBL on problems of stratospheric CAT.

Our large scale computations are sponsored by a DoD HPC Grand Challenge Grant, focused on ABL Propagation Codes and Atmospheric-Optical Turbulence; co-investigators include Dr. Frank Ruggiero (AFRL/VSBL) and Dr. Joseph Werne (Northwest Research Associates, CO). We have made several presentations at ABL-related workshops and conferences (see list below).

We have cooperated with NAVO MSRC visualization team on 3d animated graphics of our turbulent data sets. An article has been published in the Spring 2003 DOD HPC *Navigator* journal.

5 Personnel Supported

- Prof. Alex Mahalov, Department of Mathematics, Arizona State University
- Prof. Basil Nicolaenko, Department of Mathematics, Arizona State University
- Prof. H.J.S. Fernando, Center for Environmental Fluid Dynamics, Arizona State University
- Dr. Binson Joseph, Post Doctoral Fellow, Arizona State University
- Dr. Frank Tse, Post Doctoral Fellow, Arizona State University
- Prof. Anatoli Babin, Collaborator, University of California, Irvine
- Graduate Students Jamshed Ghoush, Bongsik Kim and Markus Trahe.

6 Selected Publications on Atmospheric Dynamics

1. A. Mahalov, B. Nicolaenko, and K. L. Tse, Quasi-equilibrium dynamics of shear-stratified turbulence in a model tropospheric jet, *Journal of Fluid Mechanics*, **496**, p. 73-103, 2003.
2. B. Joseph, A. Mahalov, B. Nicolaenko, and K. L. Tse, Variability of turbulence and its outer scales in a tropopause jet, *Journal of the Atmospheric Sciences*, **61**, No. 6, p. 621-643, 2004.

3. B. Joseph, A. Mahalov, B. Nicolaenko, and K. L. Tse, High resolution DNS of jet stream generated tropopausal turbulence, *Geophysical Research Letters*, **30**, No. 10, p. 32.1-32.5 (2003).
4. A. Mahalov, B. Nicolaenko and M. Adams, Clear air and optical turbulence in a jet stream in the Airborne Laser context, *Navigator*, Spring 2003, NAVO MSRC, p. 16-21 (2003).
5. M. Farge, A. Mahalov, B. Nicolaenko, and K. L. Tse, Vortex tubes in shear-stratified turbulence, Special Issue on “Tubes, Sheets and Singularities in Fluid Dynamics”, Kluwer Academic Publishers, p. 21-32 (2002).
6. A. Babin, A. Mahalov, and B. Nicolaenko, Singular oscillating limits of stably stratified three-dimensional Euler and Navier-Stokes equations and ageostrophic wave fronts, in the monograph *Large-Scale Atmosphere-Ocean Dynamics*, Cambridge University Press, Volumes 1 and 2, p. 126-201 (2002).
7. A. Mahalov, B. Nicolaenko, K. L. Tse and B. Joseph, High resolution DNS of shear-convective turbulence and its implications to second-order parameterizations, *Theoretical and Computational Fluid Dynamics*, **17**, No. 5-6, 2003.
8. A. Mahalov, B. Joseph, B. Nicolaenko and K.-L. Tse (2004), Eddy-Mixing in Jet-Stream Turbulence under Stronger Stratification, *Geophys. Research Lett.*, vol. 23, L23111-23115.

Normalized (Brunt–Vaisala freq) $\wedge 2$ at $y=3.1$

case5; alpha=8

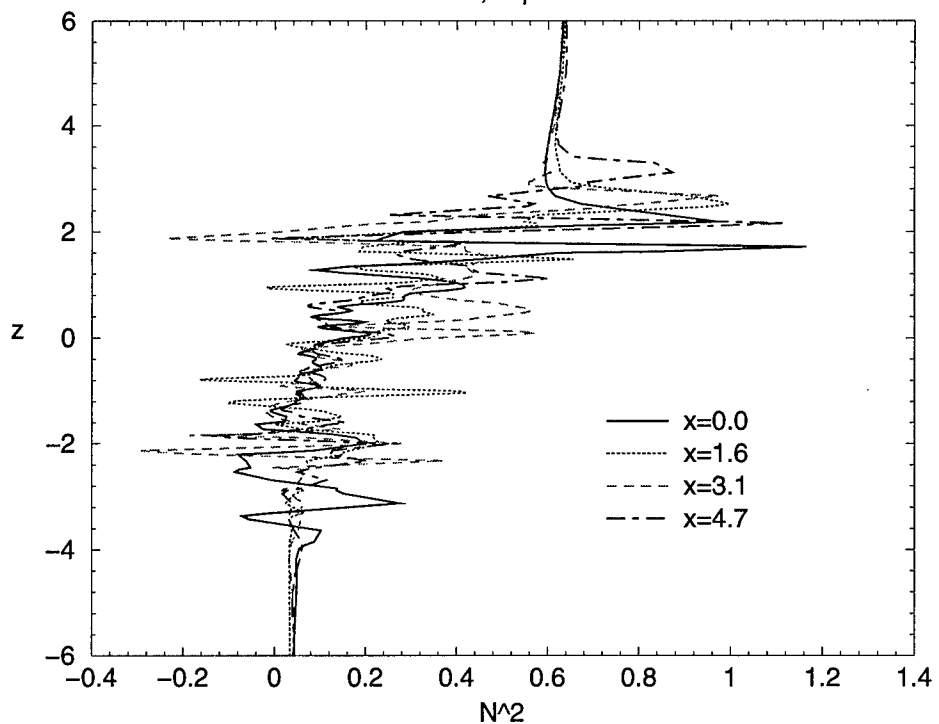


Figure 1: Normalized Brunt-Vaisala frequency N^2 at section $y = 3.1$

Local Gradient Richardson Number - high
resolution case.

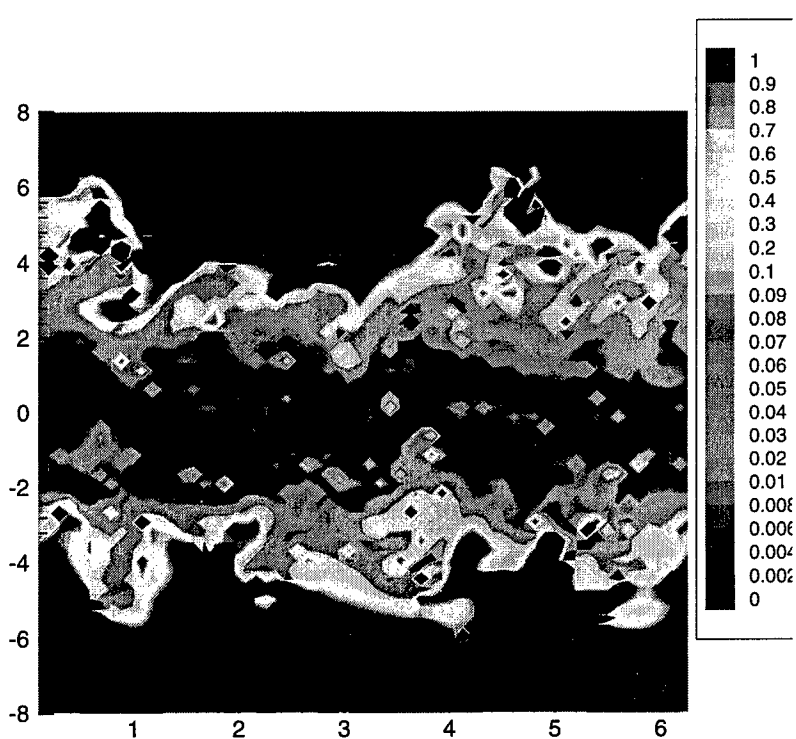


Figure 2: Local gradient Richardson number- high resolution case

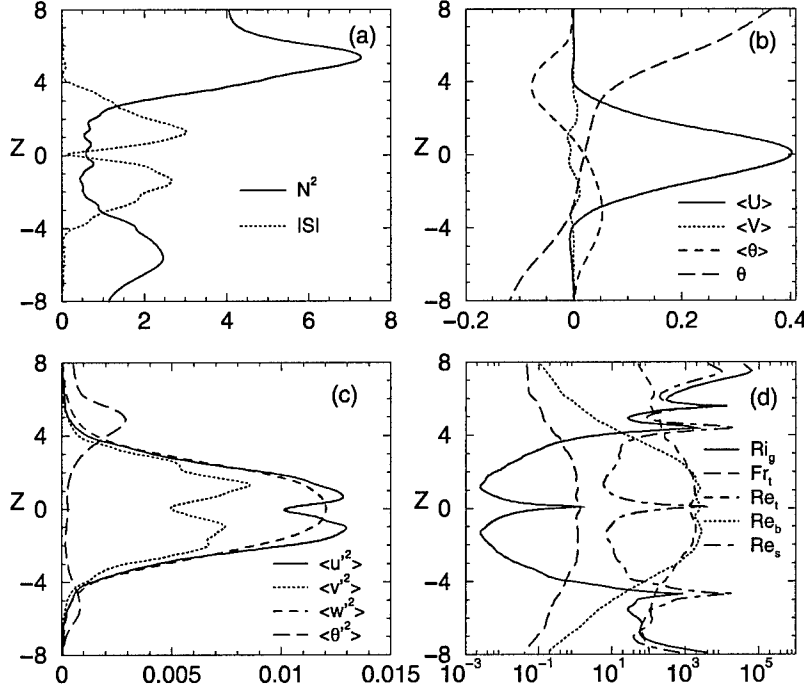


Figure 3: Vertical profiles of horizontally averaged (mean) quantities in the quasi-equilibrium turbulent jet: (a) squared Brunt-Väisälä frequency N^2 (normalized by N_o^2) (solid), absolute wind shear $|S|$ (dotted) (b) streamwise mean velocity $\langle U \rangle$ (solid), spanwise mean velocity $\langle V \rangle$ (dotted), mean of perturbation temperature $\langle \theta \rangle$ (dashed), total mean temperature $\bar{\theta}$ (long-dashed) (c) streamwise velocity variance $\langle |u'|^2 \rangle$ (solid), spanwise velocity variance $\langle |v'|^2 \rangle$ (dotted), vertical velocity variance $\langle |w'|^2 \rangle$ (dashed), temperature variance $\langle |\theta'|^2 \rangle$ (long-dashed) (d) gradient Richardson number Ri_g (solid), turbulent Froude number Fr_t (long-dashed), turbulent Reynolds number Re_t (dashed), buoyancy Reynolds number Re_b (dotted), and shear Reynolds number Re_s (dash-dotted) (e) vertical heat flux $\langle \theta' w' \rangle$ (solid), vertical momentum flux $\langle u' w' \rangle$ (dotted), horizontal heat flux $\langle \theta' u' \rangle$ (dashed) (f) TKE dissipation ϵ (solid), and dissipation of temperature variance ϵ_θ (dotted). The dashed line in (a) and dash-dotted line in (b) are, respectively, the basic state squared Brunt-Väisälä frequency N_b^2 (normalized by N_o^2) and the momentum source Π_U .

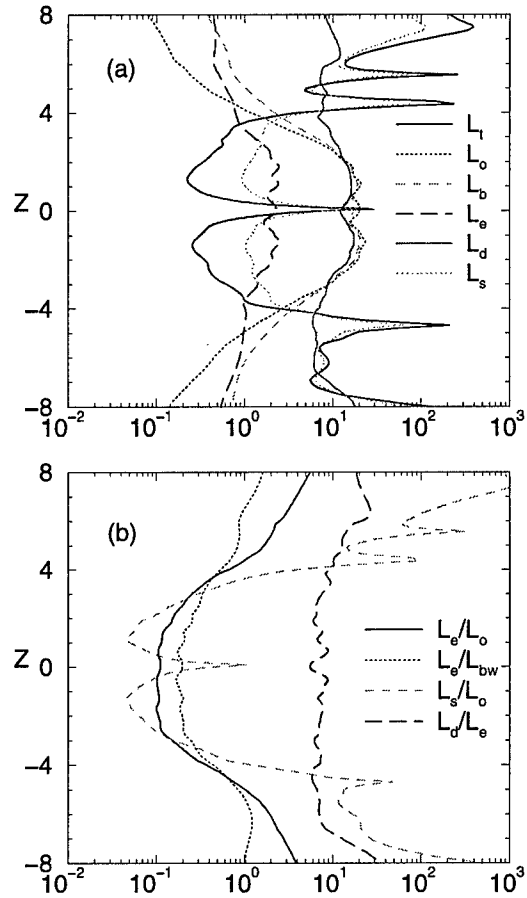


Figure 4: (a) Vertical profiles of length scales L_t (solid-black), L_o (dotted-red), L_b (dashed-green), L_e (long-dashed-blue), L_k (dash-dotted-magenta), L_d (thick solid-indigo), and L_s (thick dash-dotted-orange) (b) vertical profiles of length scale ratios L_e/L_o (solid), L_e/L_{bw} (dotted), L_s/L_o (dashed), L_d/L_e (long-dashed).

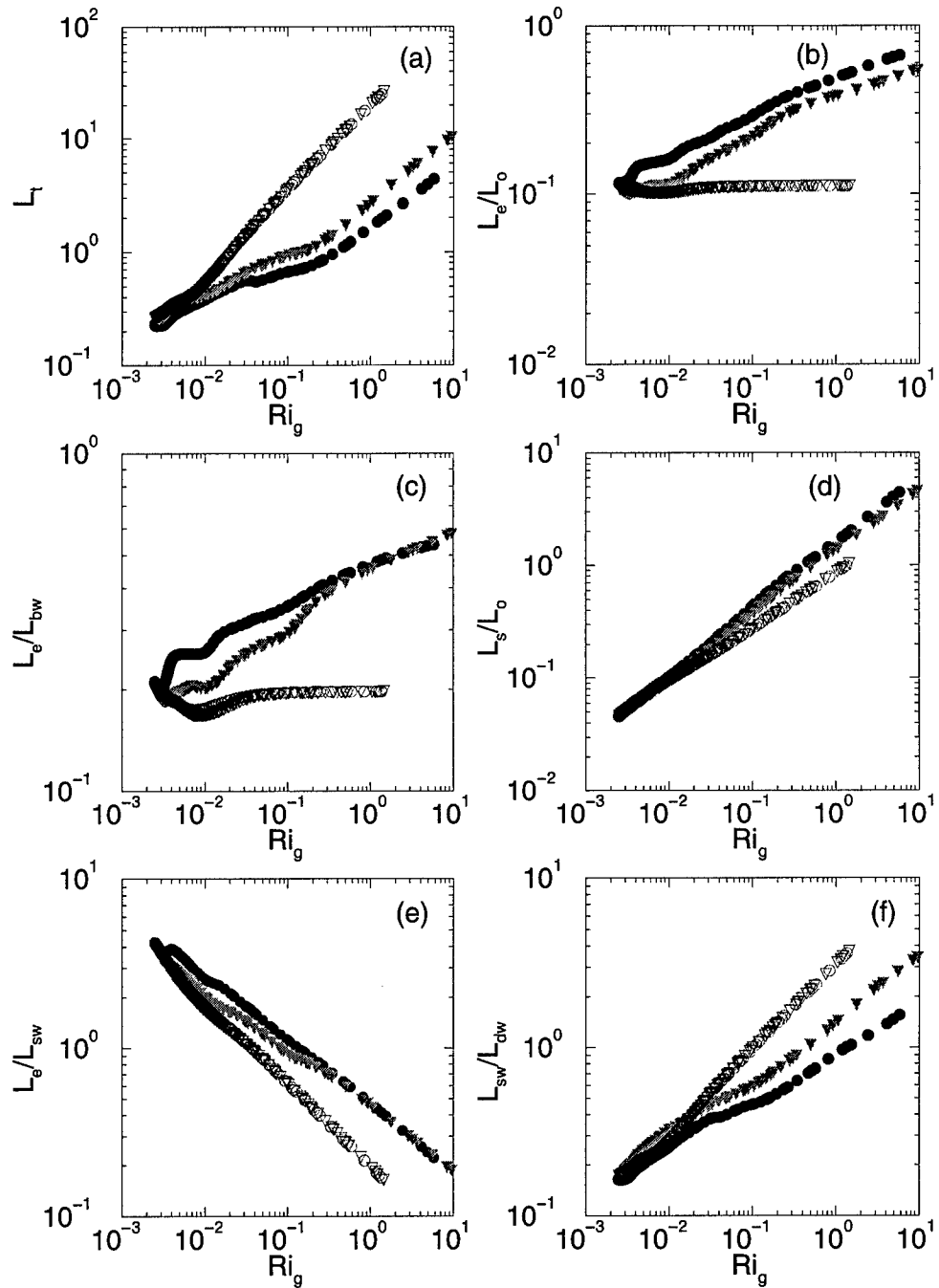


Figure 5: Scalings, with Ri_g , of some length scales/ratios: (a) L_t (b) L_e/L_o (c) L_e/L_{bw} (d) L_s/L_o (e) L_e/L_{sw} (f) L_{sw}/L_{bw} . Circles (black and red) are points on the upper flank of the jet; inverted triangles (green and blue) for those on the lower jet flank. Filled symbols (black and green) represent points in the outer scaling region (outside of IP); open symbols (red and blue) are points in the inner scaling region (between IP levels).

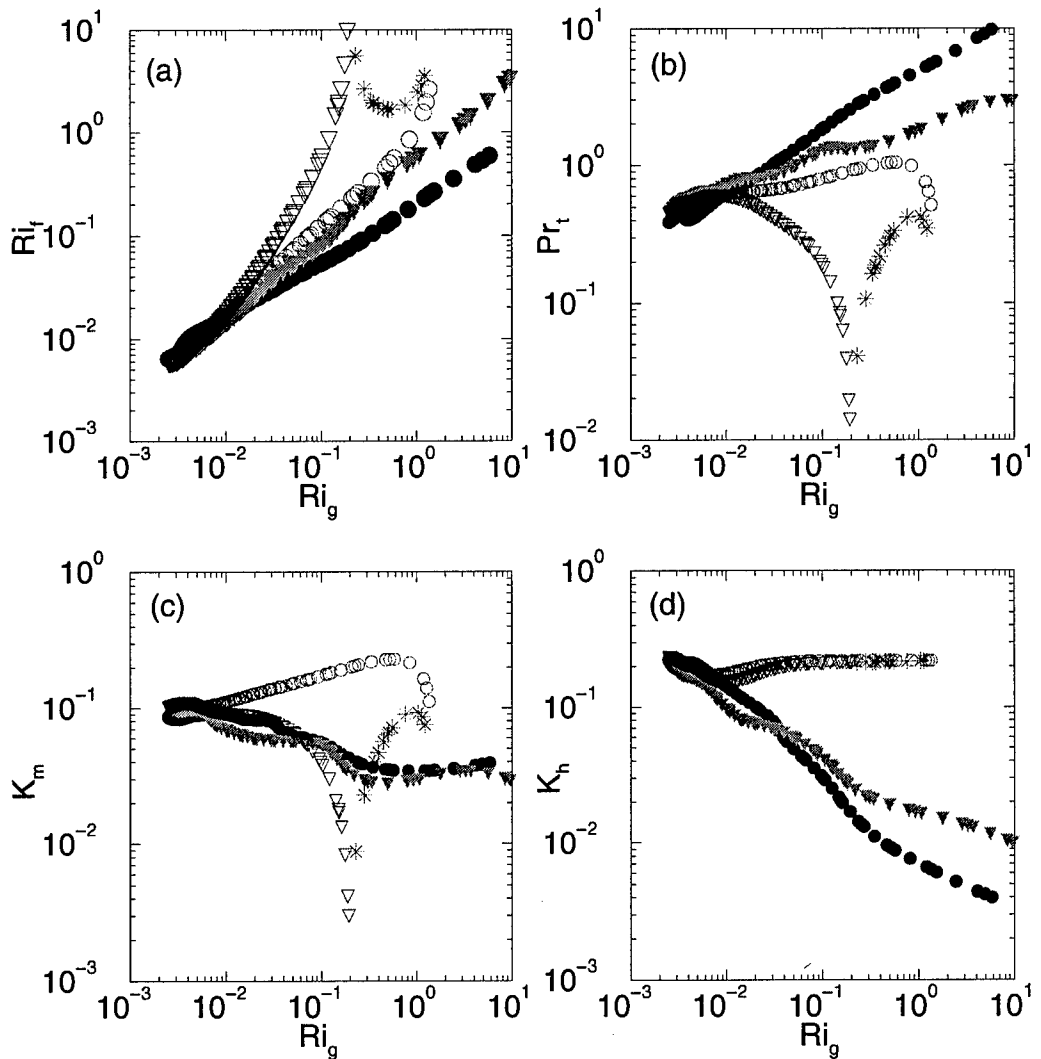


Figure 6: Scalings, with Ri_g , of common eddy mixing parameters: (a) Ri_f (b) Pr_t (c) K_m (d) K_h . Symbols as in the previous figure. The 'star' symbols denote the tiny branch with countergradient momentum flux.

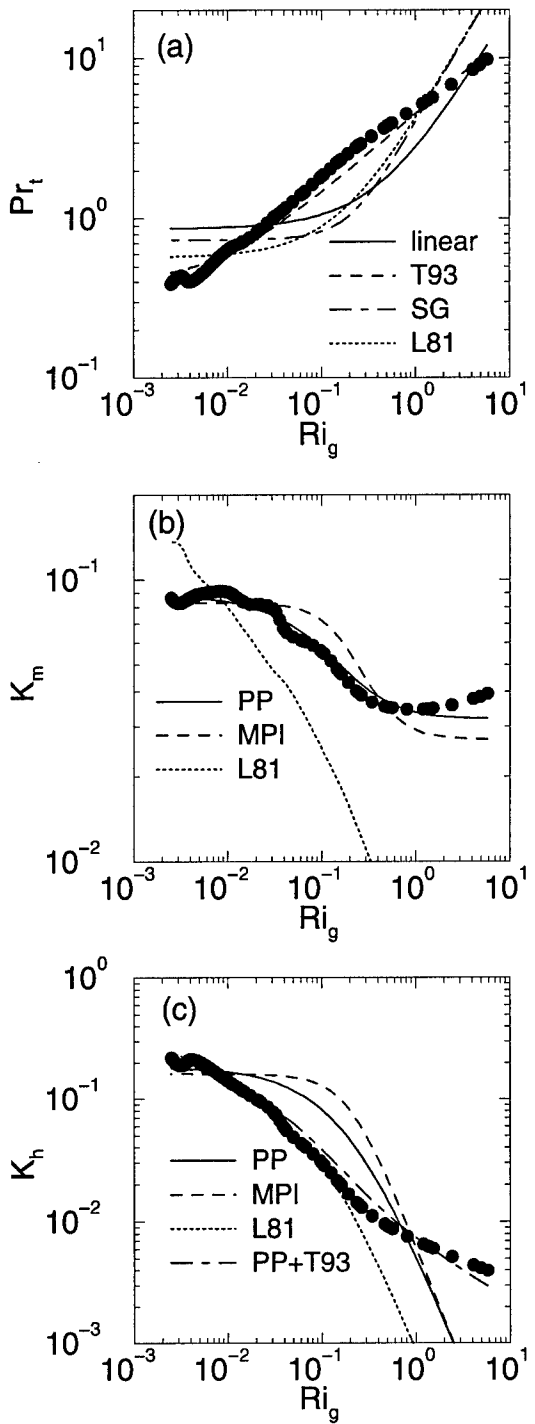


Figure 7: Scalings of eddy mixing parameters along the (upper) outer region (cf. Fig. 2), and some model fits: (a) Pr_t (b) K_m (c) K_h . Legends are described in the text and Table 6. The abbreviations stand for models: *linear* (cf. Kim and Mahrt 1992), *T93* (Tjernström 1993), *SG* (Schumann and Gerz 1995), *PP* (Pacanowski and Philander 1981), *MPI* (Max Plank Institute scheme; Latif et al. 1994), and *L81* (Louis et al. 1981).

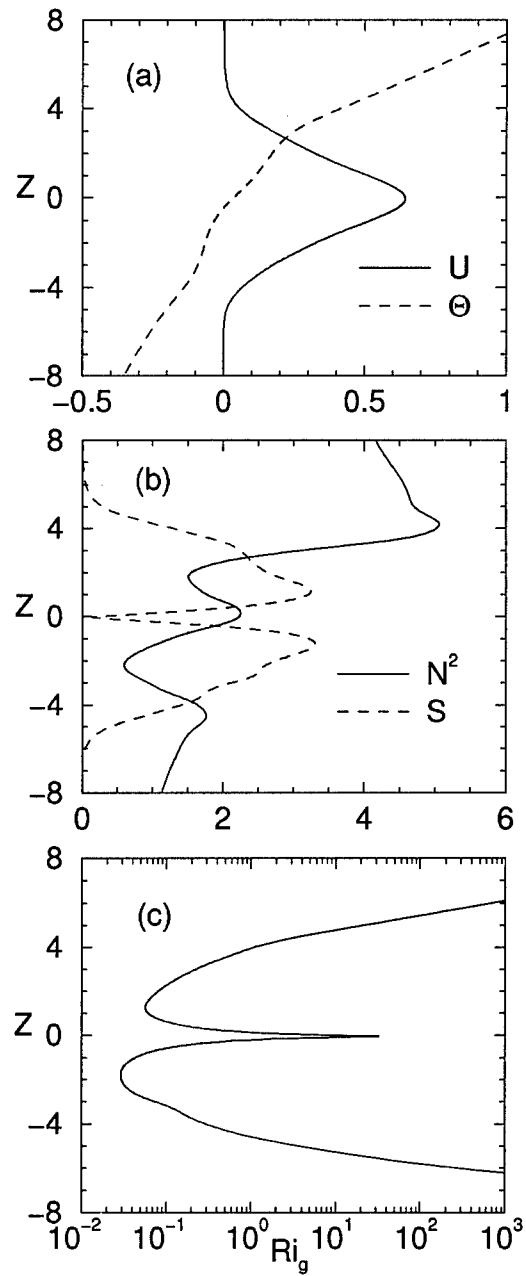


Figure 8: Vertical profiles of turbulent mean quantities at quasi-equilibrium: (a) mean streamwise velocity (U) and total mean potential temperature (Θ) (b) squared Brunt-Väisälä frequency (N^2 ; normalized by N_o^2) and mean horizontal velocity shear (S) (c) gradient Richardson number (Ri_g).

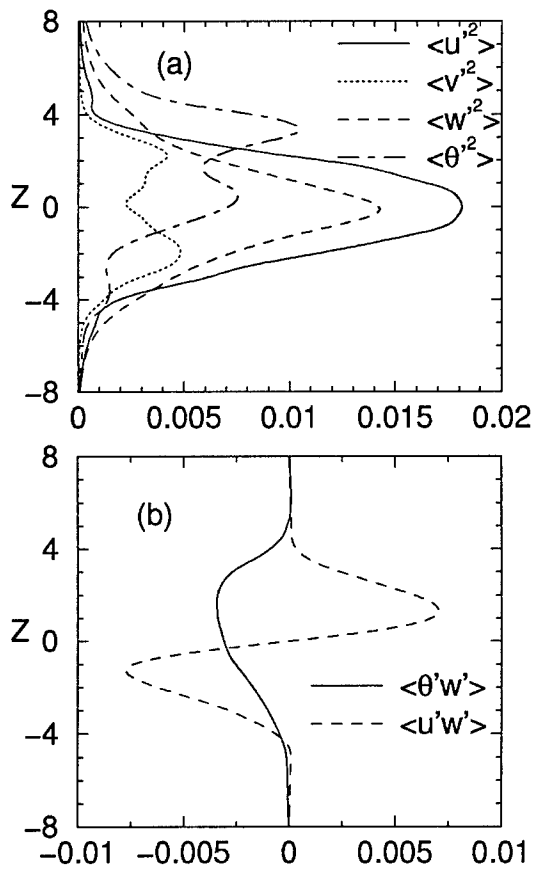


Figure 9: Vertical profiles of turbulent fluctuating quantities at quasi-equilibrium: (a) turbulent variances: $\langle u'^2 \rangle$, $\langle v'^2 \rangle$, $\langle w'^2 \rangle$, and $\langle \theta'^2 \rangle$ (b) turbulent fluxes: $\langle \theta'w' \rangle$, $\langle u'w' \rangle$.

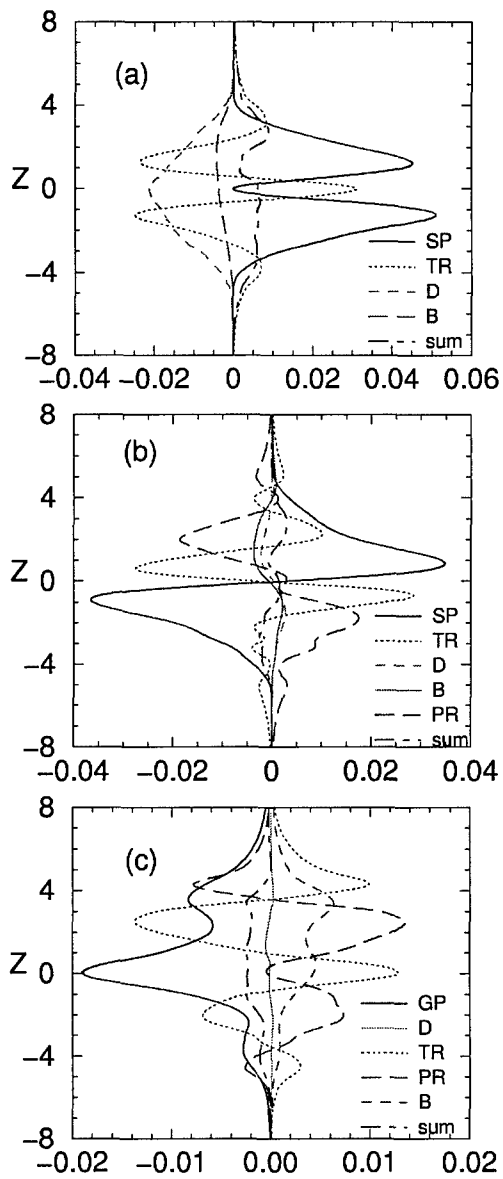


Figure 10: Budgets of turbulent quantities: (a) turbulent kinetic energy q^2 , (b) momentum flux $\langle u'w' \rangle$, (c) heat flux $\langle \theta'w' \rangle$.

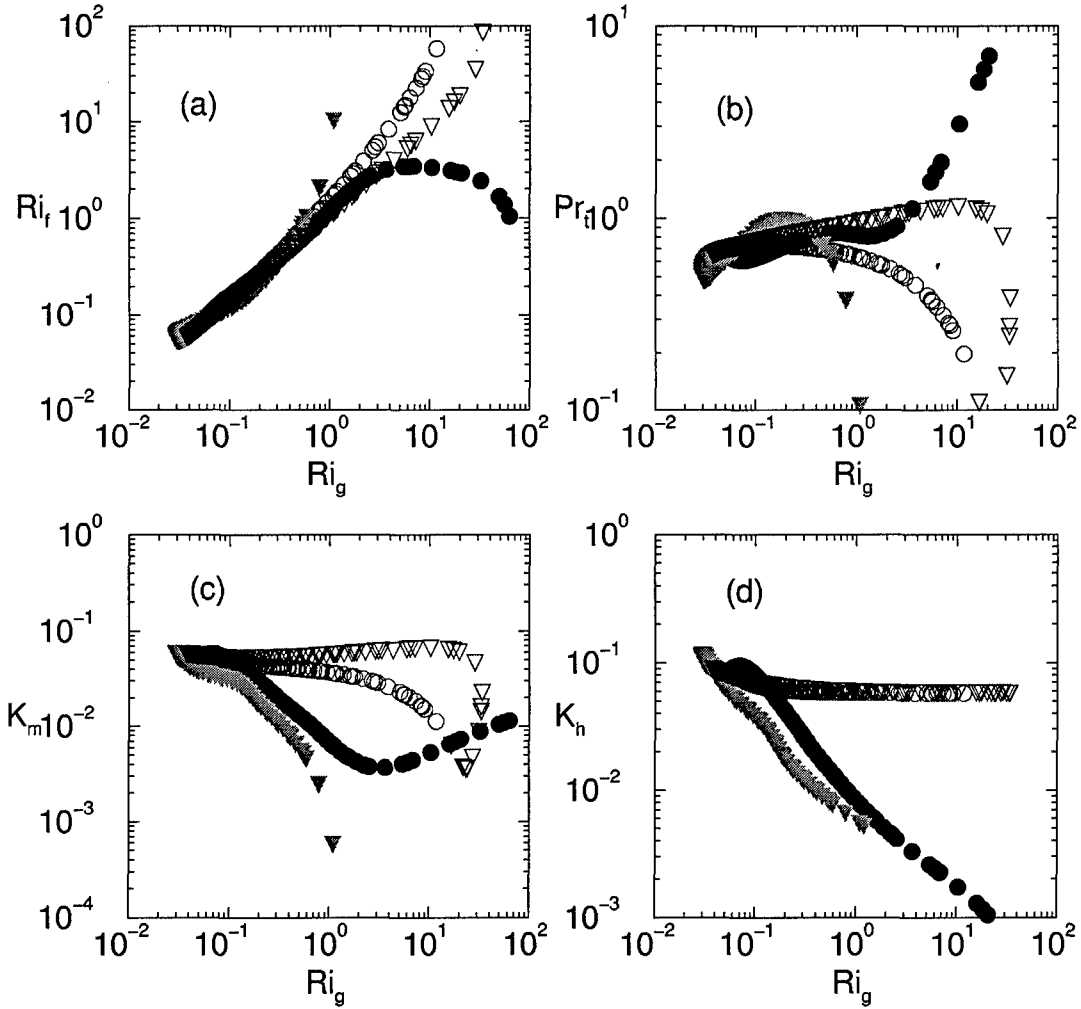


Figure 11: Scalings, with Ri_g , of turbulent eddy mixing parameters: (a) Ri_f (b) Pr_t (c) K_m (d) K_h . Circles (black and red) are points on the upper flank of the jet; inverted triangles (green and blue) for those on the lower jet flank. Filled symbols (black and green) represent points in the outer scaling region (outside of IP); open symbols (red and blue) are points in the inner scaling region (between IP levels).

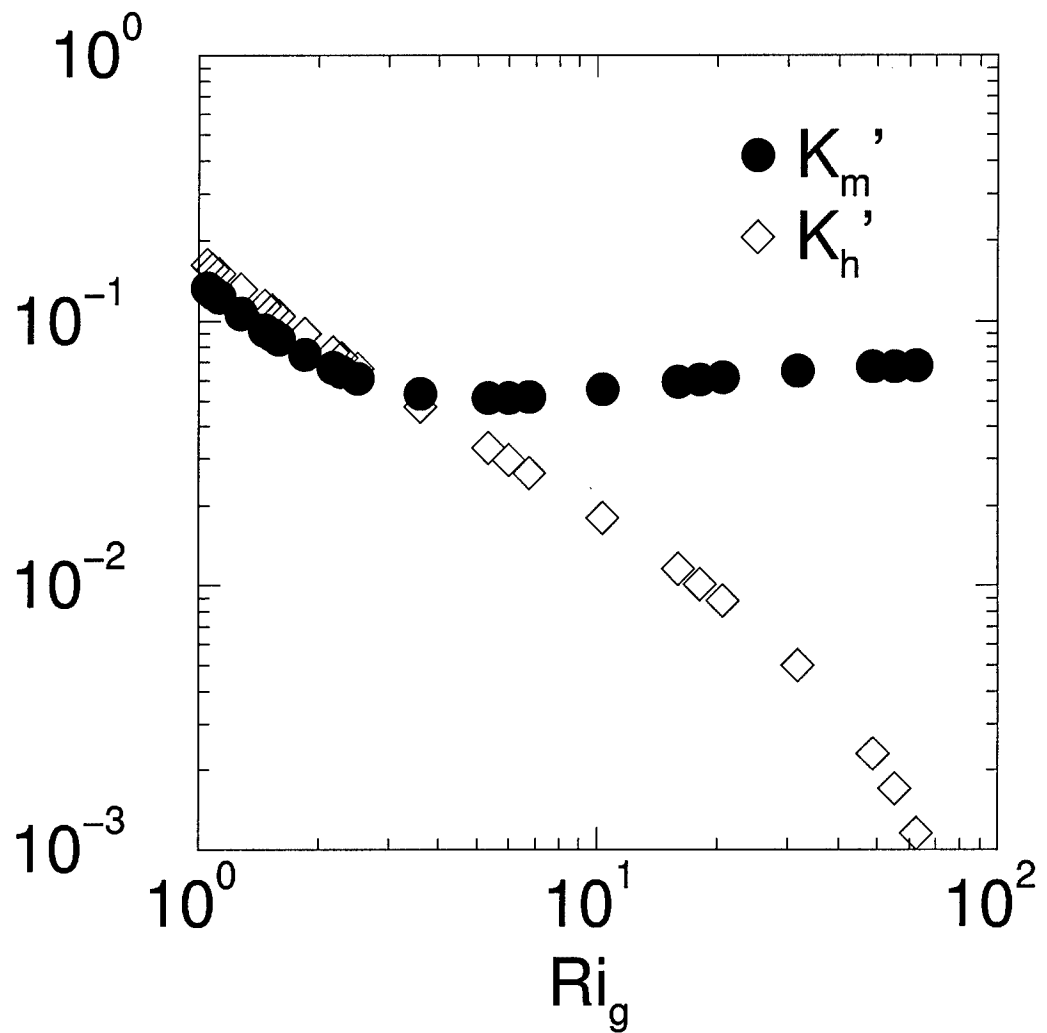


Figure 12: Scalings of turbulent eddy mixing coefficients K_m and K_h (normalized by $\langle w'^2 \rangle / S$) with Ri_g along the upper-outer branch.

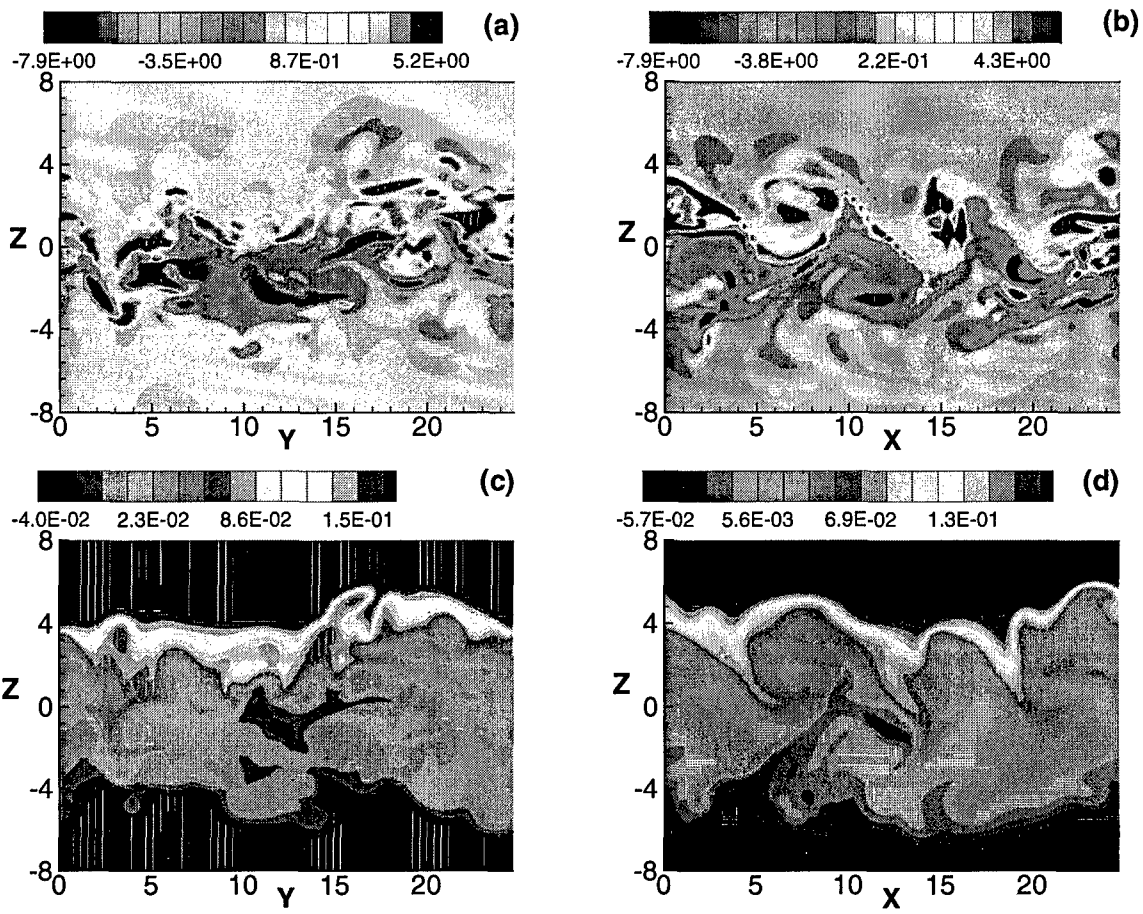
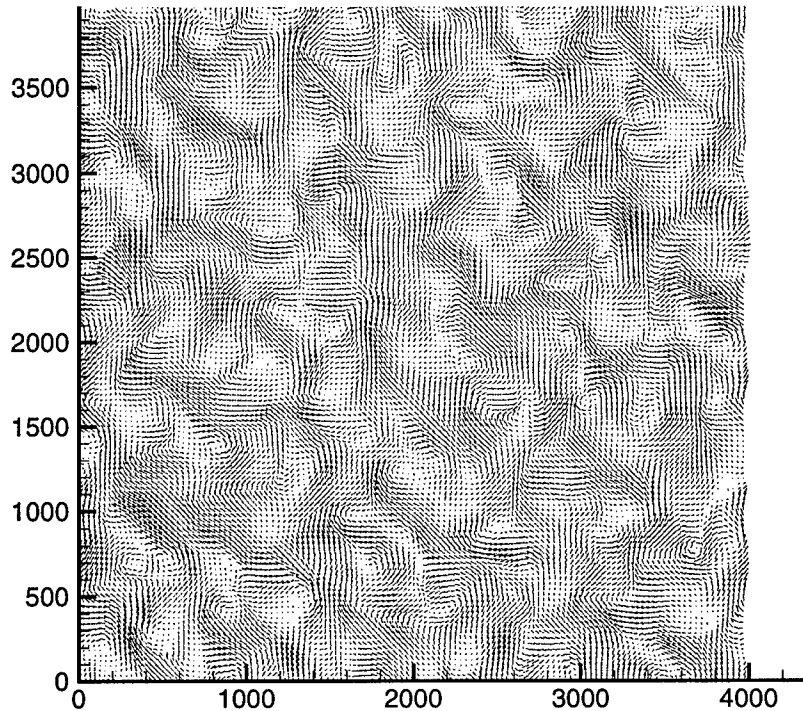


Figure 13: Vertical cross-sections of instantaneous fields: (a) normalized spanwise vorticity on central $Y - Z$ plane, (b) spanwise vorticity on central $X - Z$ plane, (c) normalized total temperature in the central $Y - Z$ plane, (d) total temperature in the central $X - Z$ plane (Joseph, Mahalov, Nicolaenko and Tse 2004).

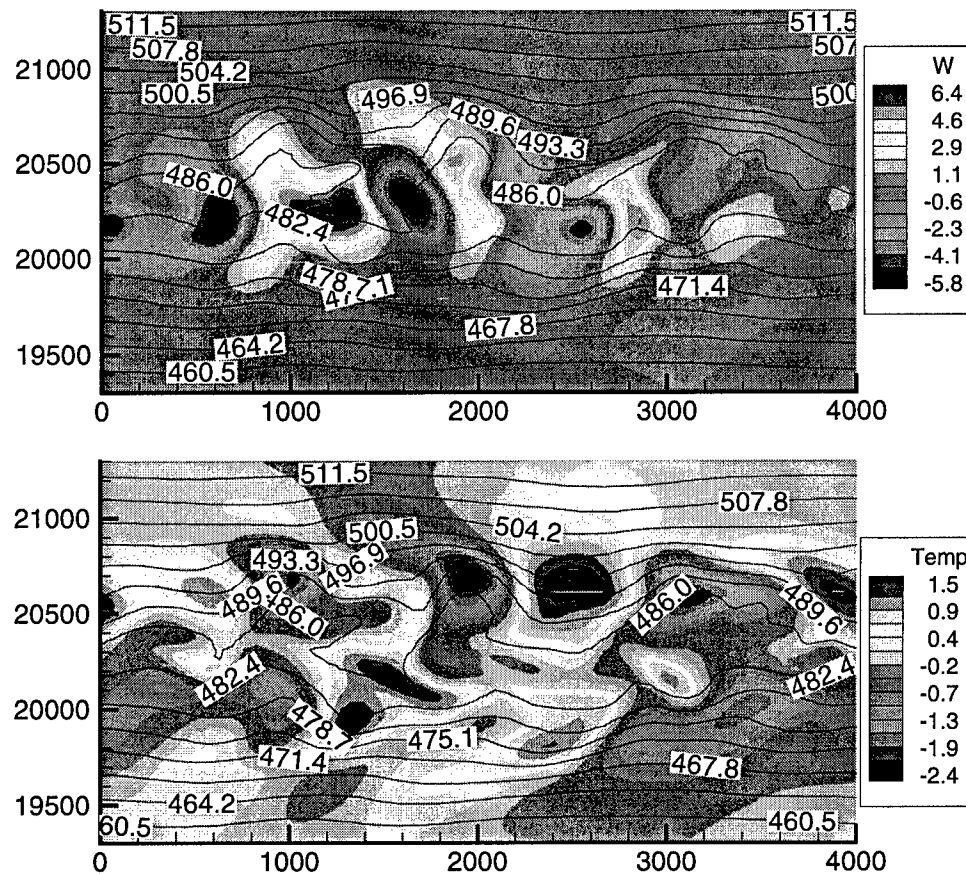
Velocity projection on a horizontal plane at 20.3km



The horizontal axis (in m) represents the east-west direction and the vertical axis (in m) represents the north-south direction. Stratospheric CAT layer at 20,300m altitudes is dominated by strong energetic eddies with typical horizontal scale $\sim 500m$

Figure 14: Velocity projection on a horizontal plane at 20.3km

Vertical velocity (m/s), temperature perturbation and potential temperature (K) surfaces in a randomly chosen vertical cross section.



Top - vertical velocity (colour contours) with total potential temperature (line contours); bottom - temperature fluctuation (colour contours) with total potential temperature (line contours).

Figure 15: Vertical velocity (m/s), temperature perturbation and potential temperature (K) surfaces in a randomly chosen vertical cross section

Vertical velocity and temperature contours in a horizontal cross section at $z = 20.3\text{km}$.

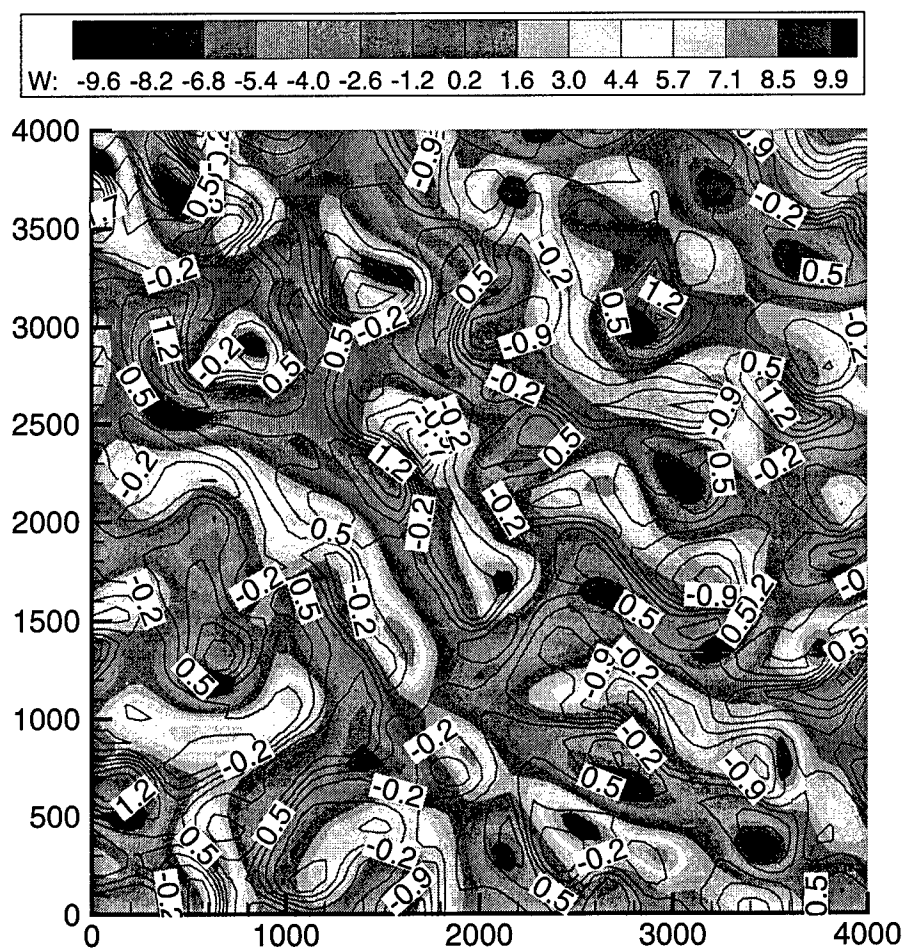


Figure 16: Vertical velocity and temperature contours in a horizontal cross section at $z=20.3\text{km}$

Vertical velocity and vertical vorticity contours in a horizontal cross section at $z = 20.3\text{km}$.

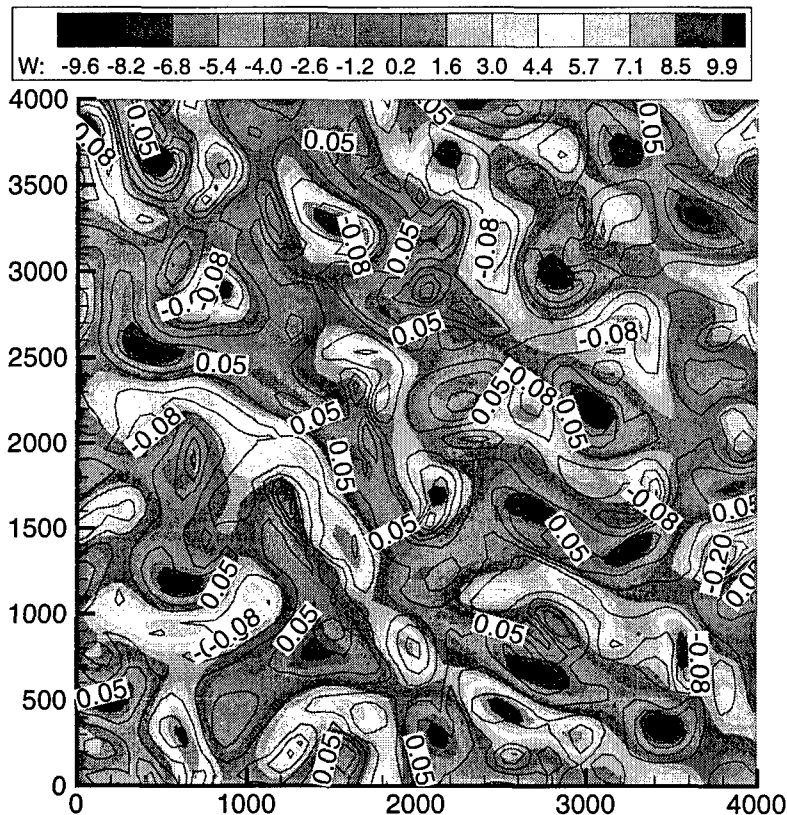


Figure 17: Vertical velocity and vertical vorticity contours in a horizontal cross section at $z=20.3\text{km}$

0309

REPORT DOCUMENTATION PAGE

Public reporting burden for this collection of information is estimated to average 1 hour per response, including the time for reviewing ir
the data needed, and completing and reviewing this collection of information. Send comments regarding this burden estimate or any o
information, including suggestions for
reducing this burden to Washington Headquarters Services, Directorate for Information Operations and Reports, 1215 Jefferson Davis Highway, Suite 1204, Arlington, VA 22202-4302, and to the Office of
Management and Budget, Paperwork Reduction Project (0704-0188), Washington, DC 20503

1. AGENCY USE ONLY (Leave blank)	2. REPORT DATE 20 July 2005	3. REPORT TYPE AND DATES COVERED FINAL TECHNICAL REPORT 01 Jan 2002 - 31 Jan 2005
4. TITLE AND SUBTITLE Statistics and Variability of Turbulence Dynamics in the Middle Atmosphere		5. FUNDING NUMBERS AFOSR G F49620-02-1-0026
6. AUTHOR(S) Alex Mahalov Basil Nicolaenko		
7. PERFORMING ORGANIZATION NAME(S) AND ADDRESS(ES) Arizona State University Tempe, AZ 85287-1603		8. PERFORMING ORGANIZATION REPORT NUMBER N/A
9. SPONSORING / MONITORING AGENCY NAME(S) AND ADDRESS(ES) Air Force Office of Scientific Research AFOSR/PKC 875 North Randolph Road Arlington, VA 22203		10. SPONSORING / MONITORING AGENCY REPORT NUMBER <i>NM</i>
11. SUPPLEMENTARY NOTES		
12a. DISTRIBUTION / AVAILABILITY STATEMENT Unrestricted Public Availability and Release		12b. DISTRIBUTION CODE
13. ABSTRACT (Maximum 200 Words) The project falls within the realm of the USAF Airborne Laser (ABL) Program. One of the challenges of the ABL Atmospheric Decision Aid (ADA) program is the development of codes for the prediction and parameterization of the refractive index structure function in the middle atmosphere under conditions of non-homogeneous, anisotropic turbulence for shear-stratified atmospheric flows. Variability of flow regimes and turbulence scalings in inhomogeneously stratified tropopause jets is investigated through high-resolution, three-dimensional numerical simulations on massively parallel architectures. Multi-valued scaling branches, with respect to the local gradient Richardson number are shown to occur in several turbulent quantities such as variances, fluxes, mixing efficiency, outer scales and their ratios. The vertical levels corresponding to the maximal shearing in the quasi-equilibrium turbulent mean jet velocity profile is identified as the best criterion for branch switching along each of the scaling curves. Regime transitions, for the jet-induced inhomogeneously stratified turbulence near the tropopause, are identified based on crossovers in various turbulence outer scales. As one traverses away from the center of the jet, the following sequence of regime transitions may be identified: shear-dominated, buoyancy-affected, buoyancy-dominated. We also find that several of the turbulence scaling relations undergo a significant change at the transition from the buoyancy-affected to the buoyancy-dominated regime. Such multiple scalings impact on prediction of optical turbulence and parameterizations in mesoscale weather codes.		
14. SUBJECT TERMS Atmospheric Turbulence, Optical Turbulence, Shear Stratified Flows, Optical Refractive Index Variability		15. NUMBER OF PAGES 44
		16. PRICE CODE
17. SECURITY CLASSIFICATION OF REPORT UNCLASSIFIED	18. SECURITY CLASSIFICATION OF THIS PAGE UNCLASSIFIED	19. SECURITY CLASSIFICATION OF ABSTRACT UNCLASSIFIED
20. LIMITATION OF ABSTRACT		

NSN 7540-01-280-5500

Standard Form 298 (Rev. 2-89)
Prescribed by ANSI Std. Z39-18
298-102

7-26-05